

Numerical method for strongly variable-density flows at low Mach number: flame-sheet regularisation and a mass-flux immersed boundary method

Matheus P. Severino^{a,*}, Fernando F. Fachini^b, Elmer M. Gennaro^c, Daniel Rodríguez^d, Leandro F. Souza^a

^a*Instituto de Ciências Matemáticas e de Computação, Universidade de São Paulo
13566-590 São Carlos – São Paulo, Brazil*

^b*Grupo de Mecânica de Fluidos Reativos, Instituto Nacional de Pesquisas Espaciais
12630-000 Cachoeira Paulista – São Paulo, Brazil*

^c*Departamento de Engenharia Aeronáutica, Universidade Estadual Paulista
13876-750 São João da Boa Vista – São Paulo, Brazil*

^d*Escuela Técnica Superior de Ingeniería Aeronáutica y del Espacio, Universidad Politécnica de Madrid
28040 Madrid – Madrid, Spain*

Abstract

A low-Mach-number flow, in the laminar regime, has intrinsically two characteristic spatial scales for a given time scale, or two characteristic temporal scales for a given spatial scale, and these dual scales are very different due to the disparity between the flow and acoustic speed. Therefore low-Mach-number flows impose mathematical and computational challenges in their description. Standard numerical methods for compressible flows, which are typically designed for problems with a single dominant spatial and temporal scale, require alternative approaches such as preconditioning techniques or solvers tailored for low-Mach-number equations. The present work introduces a simplified fluid dynamics model for flows at low Mach number, based on the fractional time-step method. The proposed approach is suitable for handling strong temperature gradients and thermal diffusion, as encountered in combustion systems. To address discontinuities at the flame front in reacting-flow cases, due to the hypothesis of infinitely fast chemistry, a regularisation procedure is employed. Additionally, the immersed boundary method (IBM) is extended to handle mass flux across the boundary surface, enabling simulations of fuel ejection from an arbitrary burner geometry, using a convenient Cartesian grid. The numerical method utilises a predictor-corrector scheme for time integration on a collocated grid, with flux interpolation to prevent numerical pressure oscillations (“odd-even decoupling”). Relevant test cases are used to verify the methods and their implementations, demonstrating correctness and robustness.

Keywords: Projection method, Fractional step method, Penalisation method, Collocated grid, Reacting flows, Combustion, Diffusion flames

*Corresponding author

Email addresses: matheus.severino@usp.br (Matheus P. Severino), fernando.fachini@inpe.br

1. Introduction

Low Mach number flows, in which the characteristic flow speed is much smaller than the speed of sound, are prevalent in natural phenomena and engineering applications [1, 2]. They are commonly found in fields such as Combustion, Meteorology, and Geophysics [3, 4]. These flows are mathematically characterised by a small Mach number, which is a scaling factor for the pressure term, relating hydrodynamic and thermodynamic contributions. The low Mach number limit represents a singular limit [5–8], meaning that the mathematical nature of the equations undergoes a significant transformation as the Mach number approaches zero. This characteristic presents challenges in both analytical [6, 9] and numerical treatments [8, 10]. The singular nature introduces disparate scales into the problem – a short time scale, associated with fast-propagating acoustic waves, and a large time scale, related to much slower fluid flow [1] –, leading to a stiff system of equations. As a result, standard compressible flow solvers, become inaccurate and inefficient at low Mach numbers [11, 12]. Explicit methods require impractically small time steps, due to the Courant–Friedrichs–Lewy (CFL) condition, which is constrained by the speed of sound in the system. Although implicit methods allow for larger time steps, they face challenges with ill-conditioned matrices.

The most direct procedure to handling low Mach number flows involves applying preconditioning techniques to a compressible solver, improving the conditioning of the system [13]. This method is ideal for flows with significant local variations in the Mach number. A second approach is to employ a solver specifically designed to solve the low-Mach-number asymptotic equations [1], making it more effective and accurate for cases involving purely low Mach number flows. Within this latter category, the artificial compressibility [14] and projection (or fractional time-step) methods [15, 16] are notable. They were initially developed for the particular case of incompressible flows (i.e, low Mach number flows at the quasi-isentropic or quasi-adiabatic thermodynamic limit [8, 9]).

The strategy of the artificial compressibility method is to introduce artificial subsonic acoustic waves that propagate without influencing the fluid velocity [17]. This approach recuperates the physical-mathematical structure of a compressible system, explicit in time and local in space. However, for accurate unsteady simulations, it usually requires a dual-time stepping approach with sub-iterations in artificial time (towards the steady-state solution), for each physical time step [18]. Additionally, the selection of the artificial wave propagation speed is not a trivial task. A comprehensive analysis of the artificial compressibility method, including its physical significance, is presented in [8], and an extension for non-isothermal flows can be found in [17].

The projection method, also known as the fractional time-step method, is a type of operator-splitting technique [19]. It decomposes the original equation (operator) into independent sub-equations (operators). Each sub-equation is solved separately, and the solution to the original equation is, then, constructed by combining them. The primary advantage of this approach is that solving each sub-equation individually is, in general, much more straightforward and computationally efficient than solving the original problem directly, although it does introduce splitting

(Fernando F. Fachini), elmer.gennaro@unesp.br (Elmer M. Gennaro), daniel.rodriquez@upm.es
(Daniel Rodríguez), lefraso@icmc.usp.br (Leandro F. Souza)

errors. An interesting perspective is to interpret this method as a block LU decomposition [20, 21]. This view clarifies the implied approximations and helps avoid the traditional confusion regarding the order of accuracy and boundary conditions for intermediate (temporary) velocity and pressure. A key advantage of the projection method over the artificial compressibility method is its ability to ensure mass conservation strictly, without relying on an artificial compressibility parameter or requiring dual-time stepping. On the other hand, the global (elliptic) nature of the hydrodynamic pressure makes its integration (by inverting a Poisson equation) the most computationally intensive part of the method.

The immersed boundary method (IBM) is a numerical technique designed to simulate fluid flows involving complex geometries, using convenient orthogonal grids. Initially introduced in the 1970s to model blood flow through heart valves [22], IBM has been widely recognised as a versatile and effective approach for addressing fluid-structure interaction problems [23]. Fundamentally, the method incorporates a volumetric forcing term into the conservation equations [24]. The specific definition and treatment of this forcing differentiate IBM into distinct methodological categories, such as continuous and discrete forcing approaches [25]. As the names suggest, a continuous forcing method incorporates the forcing term before discretising the conservation equations, making it independent of the numerical schemes. Conversely, a discrete forcing method applies the forcing term after discretisation, rendering it dependent on the specific numerical implementation. Within the continuous forcing category, penalisation (or penalty) methods model the immersed body as a porous medium [24–27], in which the forcing term acts as a damping force [26]. It was originally proposed to model natural convection in porous medium [28]. As the permeability tends to zero, the porous structure approaches an impermeable solid. Penalisation methods can be viewed as a subset of feedback methods [24], which were originally introduced in [29]. Physically, forcing terms of feedback methods are damped oscillators [24, 25, 30].

A substantial challenge revolves around modelling diverse phenomena properly. The model should adeptly encapsulate the desired physics while maintaining simplicity to allow insightful interpretation. Given this challenge, the current study endeavours to propose a model for fluid dynamics at low Mach numbers – with strong temperature gradients and thermal energy diffusion –, using a simplified formulation. To address this, a model for reacting flows at low Mach numbers is employed, assuming that the chemical reaction is much faster than the characteristic flow speed, or, equivalently, the adoption of the Burke–Schumann limit (or kinetics) [31]. Under this assumption, reactant concentrations and the system energy can be described using coupling functions – mixture fraction and excess enthalpy –, which are transported across the domain without chemical reaction [32–36]. This approach permits the numerical investigations of diffusion flames, and will be detailed later.

Despite the formal simplifications, an infinitely narrow flame presents numerical challenges. Namely, certain coefficients and derivatives exhibit a discontinuity at the flame, due to distinct behaviours within the fuel and oxidiser subdomains. To avoid numerical oscillations, associated with discontinuities, this work proposes a regularisation procedure for these properties. In addition, it introduces a novel application of the immersed boundary method by incorporating mass flux and, thus, expanding its traditional use. Specifically, the fuel ejection from a cylindrical burner, as well as the conditions of all variables at the burner surface, are prescribed using a penalisation IBM. In addition to this clear physical interpretation, as previously described, the penalisation method is

chosen because of its formal convergence results [37, 38].

Temporal integration is performed using a predictor-corrector scheme, combined with a projection method, which has proven efficient in handling strong temperature gradients [39]. To prevent odd-even decoupling – between velocity and pressure –, a flux interpolation approach is applied on a collocated grid, used for spatial discretisation.

In what follows, the text is organised as indicated: Section 2 provides a detailed explanation of the physical assumptions and the related mathematical model; Section 3 outlines the numerical method and discusses related details; Section 4 presents relevant test cases, verifying the numerical model and its computational implementation; Finally, Section 5 concludes the study with a summary of findings.

2. Physical and Mathematical Modelling

This section outlines the physical hypotheses, and the corresponding mathematical description, for modelling reacting flows at low Mach number.

2.1. A general model

Consider a fluid with a density $\hat{\rho}$, flowing at a velocity $\hat{\mathbf{v}} := [\hat{v}_1, \hat{v}_2, \hat{v}_3]^T$, under a pressure \hat{p} and with temperature \hat{T} . This fluid comprises a mixture of N chemical species, with the mass fraction of the n -th species given by $\hat{Y}_n := \hat{\rho}_n/\hat{\rho}$, in which $\hat{\rho}_n$ is the density of the n -th species for $n = 1, \dots, N$. These variables depend, in general, both on time \hat{t} and position $\hat{\mathbf{x}} := [\hat{x}_1, \hat{x}_2, \hat{x}_3]^T$. Note that the caret symbol ($\hat{\cdot}$) denotes a dimensional quantity.

The dynamics of this system, subject to buoyancy, can be described by the following set of (dimensional) partial differential equations, representing physical laws of conservation [40]:

$$\partial_{\hat{t}}\hat{\rho} + \hat{\nabla} \cdot (\hat{\rho}\hat{\mathbf{v}}) = 0, \quad (1)$$

$$\partial_{\hat{t}}(\hat{\rho}\hat{\mathbf{v}}) + \hat{\nabla} \cdot (\hat{\rho}\hat{\mathbf{v}}\hat{\mathbf{v}}) = -\hat{\nabla}\hat{p} + \hat{\nabla} \cdot \hat{\boldsymbol{\tau}} + (\hat{\rho} - \hat{\rho}_c)\hat{\mathbf{g}}, \quad (2)$$

$$\partial_{\hat{t}}(\hat{\rho}\hat{Y}_n) + \hat{\nabla} \cdot (\hat{\rho}\hat{\mathbf{v}}\hat{Y}_n) = \hat{\nabla} \cdot (\hat{\rho}\hat{D}_n\hat{\nabla}\hat{Y}_n) + \hat{\omega}_n, \quad (3)$$

$$\partial_{\hat{t}}(\hat{\rho}\hat{h}) + \hat{\nabla} \cdot (\hat{\rho}\hat{\mathbf{v}}\hat{h}) = \partial_{\hat{t}}\hat{p} + (\hat{\mathbf{v}} \cdot \hat{\nabla})\hat{p} - \hat{\nabla} \cdot \hat{\mathbf{q}} + \hat{\nabla}\hat{\mathbf{v}} : \hat{\boldsymbol{\tau}} - \sum_{n=1}^N \Delta\hat{h}_n^0\hat{\omega}_n, \quad (4)$$

supplemented by an equation of state.

Conventional notation is employed, with $\partial_{\hat{t}}$, $\hat{\nabla}$ and $\hat{\nabla} \cdot$ denoting (dimensional) partial temporal derivative, gradient and divergence operators, respectively. In addition, $\hat{\mathbf{v}}\hat{\mathbf{v}}$ is the juxtaposition representation of the dyadic product $\hat{\mathbf{v}} \otimes \hat{\mathbf{v}}$, $\hat{\boldsymbol{\tau}}$ is the viscous stress tensor, $\hat{\rho}_c$ is a characteristic density for buoyancy, $\hat{\mathbf{g}} := -\hat{g}\mathbf{e}_{x_2}$ (with $\mathbf{e}_{x_2} := [0, 1, 0]^T$) is the gravity acceleration, \hat{D}_n is the mass diffusivity of the n -th species in the mixture, $\hat{\omega}_n := \sum_m \hat{\omega}_{n,m}$ is the chemical source term (in which $\hat{\omega}_{n,m}$ is the specific production rate of the n -th species due to the m -th reaction), $\hat{h} := \int_{\hat{T}_{ref}}^{\hat{T}} \hat{c}_p d\hat{T}$ (for a reference temperature \hat{T}_{ref}) is the sensible enthalpy and $\Delta\hat{h}_n^0$ is the standard enthalpy of formation for the n -th species.

Note that specific heats of the mixture (\hat{c}_v and \hat{c}_p) are represented by the weighted average of the specific heats of each species, i.e., $\hat{c}_v := \sum_{n=1}^N \hat{c}_{v,n} \hat{Y}_n$ and $\hat{c}_p := \sum_{n=1}^N \hat{c}_{p,n} \hat{Y}_n$. In addition, while the mass fraction (\hat{Y}_n) is inherently dimensionless, it is also marked with a caret symbol to distinguish it from Y_n , which will represent its version normalised by a characteristic value.

The viscous stress tensor ($\hat{\tau}$) is given by the Navier–Poisson law, i.e.,

$$\hat{\tau} := \hat{\mu} \left[\hat{\nabla} \hat{\mathbf{v}} + \left(\hat{\nabla} \hat{\mathbf{v}} \right)^T - \frac{2}{3} \left(\hat{\nabla} \cdot \hat{\mathbf{v}} \right) \mathbf{I} \right] + \hat{\zeta} \left(\hat{\nabla} \cdot \hat{\mathbf{v}} \right) \mathbf{I}, \quad (5)$$

in which $\hat{\mu}$ is the shear viscosity, and $\hat{\zeta}$ is the bulk (or volumetric) viscosity. Moreover, the energy flux ($\hat{\mathbf{q}}$) is determined by

$$-\hat{\mathbf{q}} := \hat{\kappa} \hat{\nabla} \hat{T} - \hat{\rho} \sum_{n=1}^N \hat{h}_n \hat{D}_n \hat{\nabla} \hat{Y}_n \quad (6)$$

The first term on the right-hand side corresponds to the Fourier’s law for thermal conduction, and the second one, to the diffusion of species with distinct enthalpies (thermal capacity). In this definition, $\hat{\kappa}$ is the thermal conductivity of the mixture and \hat{h}_n is the sensible enthalpy for the n -th species. Moreover, the mass diffusion flux is given by the Fick’s law, and the thermal energy flux due to radiation is not being explicitly accounted for.

2.2. Additional assumptions

It is assumed that the gas mixture behaves like a perfect gas, leading to the adoption of the “ideal gas law”:

$$\hat{p} = \hat{\rho} \hat{T} \hat{R} / \hat{W}, \quad (7)$$

in which \hat{R} is the universal gas constant and $\hat{W} := 1 / (\sum_{n=1}^N \hat{Y}_n / \hat{W}_n)$ is the (mean) molar mass of the mixture, denoting the molar mass of the n -th species as \hat{W}_n .

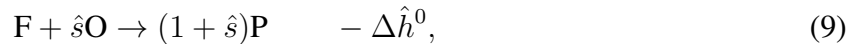
A power law is employed to represent the temperature dependence of transport coefficients [41]. Concretely, considering definitions for the numbers of Prandtl, $\text{Pr} := \hat{\mu} / (\hat{\kappa} / \hat{c}_p)$, and Lewis for the n -th species, $\text{Le}_n := [\hat{\kappa} / (\hat{\rho} \hat{c}_p)] / \hat{D}_n$, the relations $\hat{\mu} / \text{Pr} = \hat{\rho} \hat{D}_n \text{Le}_n = \hat{\kappa} / \hat{c}_p$ hold, in which

$$\frac{\hat{\kappa}}{\hat{c}_p} = \hat{A} \left(\frac{\hat{T}}{\hat{T}^*} \right)^\sigma \quad (8)$$

with $\hat{A} := 2.58 \times 10^{-5} \text{ kg}/(\text{m} \cdot \text{s})$ and $\sigma := 0.7$, for a reference temperature $\hat{T}^* = 298 \text{ K}$. Alternatively, the Sutherland’s law could be used [42].

Take into account identical specific heats for all species, i.e., $\hat{c}_v = \hat{c}_{v,i} = \hat{c}_{v,j}$ and $\hat{c}_p = \hat{c}_{p,i} = \hat{c}_{p,j}$ for each $i, j \in \{1, \dots, N\}$. Hence, the second term of energy flux, in Eq. (6), is zero [40, 41]. In addition, for a calorifically perfect gas (constant specific heats), the sensible enthalpy can be expressed as $\hat{h} = \hat{c}_p \hat{T}$.

Combustion is modelled through an irreversible, one-step global reaction between a fuel and an oxidant, as expressed symbolically by:



\hat{s} represents the stoichiometric coefficient in terms of mass, i.e., to react with one unit of fuel ('F') mass – producing $(1 + \hat{s})$ units of product ('P') mass and releasing heat $\Delta\hat{h}^0$ –, \hat{s} units of oxidiser ('O') mass are required. Similarly to the case of the mass fraction (\hat{Y}_n), it is emphasised that the parameter \hat{s} is dimensionless. However, it is introduced with a hat to distinguish it from its normalised version (s), found during the nondimensionalisation procedure. Therefore, considering $n = 1$ for fuel, $n = 2$ for oxidiser and $n = 3$ for products,

$$\hat{\omega}_n := c_n \hat{\omega}_1 \quad (10)$$

in which $c_n = 0$ for an inert n -th species (i.e., for $n \neq 1, 2, 3$), and $c_1 = 1$, $c_2 = \hat{s}$ and $c_3 = -(1 + \hat{s})$, since $\hat{\omega}_1 = \hat{\omega}_2/\hat{s} = -\hat{\omega}_3/(1 + \hat{s})$. Also, $\sum_{n=1}^N \Delta\hat{h}_n^0 \hat{\omega}_n = \hat{\omega}_1 \sum_{n=1}^N c_n \Delta\hat{h}_n^0 = \Delta\hat{h}^0 \hat{\omega}_1$, by definition. Moreover, an Arrhenius equation models the reaction rate, viz.,

$$\hat{\omega}_1 = \hat{\rho} \hat{B} \hat{Y}_1 \hat{Y}_2 e^{-\hat{E}/(\hat{R}\hat{T})} \quad (11)$$

in which \hat{B} is a pre-exponential factor, and \hat{E} is the activation energy for the chemical reaction.

These assumptions on chemical reaction, combined with the supposition of constant mean molar mass ($\hat{W} = \text{const.}$) – i.e., the fluid is a homogeneous mixture in whole domain –, permits the description of the system dynamics in terms of only two species, fuel (\hat{Y}_1) and oxidiser (\hat{Y}_2) [33].

Considering the previous hypotheses, numerical indices will be replaced by F (for fuel) and O (for oxidiser), to imbue them with more suggestive notation, for subsequent discussions.

2.3. Nondimensionalisation

Denoting the characteristic values with a subscript 'c', dimensionless quantities are obtained as:

$$\begin{aligned} t &:= \hat{t}/\hat{t}_c & , & \quad \mathbf{x} := \hat{\mathbf{x}}/\hat{l}_c \\ \rho &:= \hat{\rho}/\hat{\rho}_c & , & \quad \mathbf{v} := \hat{\mathbf{v}}/\hat{v}_c \\ T &:= \hat{T}/\hat{T}_c & , & \quad p := \hat{p}/\hat{p}_c \\ Y_F &:= \hat{Y}_F/\hat{Y}_{F,c} & , & \quad Y_O := \hat{Y}_O/\hat{Y}_{O,c} \\ D_F &:= \hat{D}_F/\hat{D}_{F,c} & , & \quad D_O := \hat{D}_O/\hat{D}_{O,c} \\ \mu &:= \hat{\mu}/\hat{\mu}_c & , & \quad \zeta := \hat{\zeta}/\hat{\mu}_c \\ \kappa &:= \hat{\kappa}/\hat{\kappa}_c & , & \quad c_p := \hat{c}_p/\hat{c}_{p,c} = 1 \\ s &:= \hat{s}\hat{Y}_{F,c}/\hat{Y}_{O,c} & , & \quad \Delta h^0 := \Delta\hat{h}^0 \hat{Y}_{F,c}/(\hat{c}_{p,c} \hat{T}_c) \\ \mathbf{g} &:= \hat{\mathbf{g}}/\hat{g}_c = -\mathbf{e}_{x_2} \end{aligned} \quad (12)$$

which induce dimensionless operators:

$$\partial_t := \hat{t}_c \partial_{\hat{t}} \quad , \quad \nabla := \hat{l}_c \hat{\nabla} \quad , \quad \nabla \cdot := \hat{l}_c \hat{\nabla} \cdot \quad (13)$$

The system, under these additional hypotheses and definitions, is described by the following set of dimensionless equations:

$$\text{St} \partial_t \rho + \nabla \cdot (\rho \mathbf{v}) = 0, \quad (14)$$

$$\text{St} \partial_t (\rho \mathbf{v}) + \nabla \cdot (\rho \mathbf{v} \mathbf{v}) = -\frac{1}{\tilde{\text{M}}^2} \nabla p + \frac{\text{Pr}}{\text{Pe}} \nabla \cdot \boldsymbol{\tau} + \frac{1}{\text{Fr}^2} (1 - \rho) \mathbf{e}_{x_2}, \quad (15)$$

$$\text{St } \partial_t (\rho Y_F) + \nabla \cdot (\rho \mathbf{v} Y_F) = \frac{1}{\text{Pe Le}_F} \nabla \cdot (\kappa \nabla Y_F) + \text{Da} \omega_F, \quad (16)$$

$$\text{St } \partial_t (\rho Y_O) + \nabla \cdot (\rho \mathbf{v} Y_O) = \frac{1}{\text{Pe Le}_O} \nabla \cdot (\kappa \nabla Y_O) + s \text{Da} \omega_F, \quad (17)$$

$$\begin{aligned} \text{St } \partial_t (\rho T) + \nabla \cdot (\rho \mathbf{v} T) = \frac{\gamma - 1}{\gamma} \left[\partial_t p + (\mathbf{v} \cdot \nabla) p + \tilde{\text{M}}^2 \frac{\text{Pr}}{\text{Pe}} (\nabla \mathbf{v} : \boldsymbol{\tau}) \right] + \\ + \frac{1}{\text{Pe}} \nabla \cdot (\kappa \nabla T) - \Delta h^0 \text{Da} \omega_F, \end{aligned} \quad (18)$$

together with the equation of state:

$$p = \rho T, \quad (19)$$

in which $\text{St} := (\hat{l}_c / \hat{v}_c) / \hat{t}_c$ is the Strouhal number, $\text{Pr} := \hat{\mu}_c / (\hat{\kappa}_c / \hat{c}_{p,c})$ is the Prandtl number, $\text{Pe} := \hat{l}_c \hat{v}_c / [\hat{\kappa}_c / (\hat{\rho}_c \hat{c}_{p,c})]$ is the Péclet number, $\text{Fr} := \hat{v}_c / (\hat{g}_c \hat{l}_c)^{1/2}$ is the Froude number, $\text{Le}_\eta := [\hat{\kappa}_c / (\hat{\rho}_c \hat{c}_{p,c})] / \hat{D}_\eta$ is the Lewis number for the species $\eta \in \{F, O\}$, $\text{Da} := (\hat{l}_c / \hat{v}_c) / [\hat{Y}_{O,c} \hat{B} e^{-\hat{E}/(\hat{R}\hat{T})}]^{-1}$ is the Dahmköhler number, $\gamma := \hat{c}_{p,c} / \hat{c}_{v,c}$ is the adiabatic index, $\tilde{\text{M}} := \gamma^{1/2} \text{M}$ is proportional to the Mach number $\text{M} := \hat{v}_c / (\gamma \hat{p}_c / \hat{\rho}_c)^{1/2}$.

Moreover, the viscous stress tensor ($\boldsymbol{\tau}$) is now expressed as

$$\boldsymbol{\tau} = \kappa \left[\nabla \mathbf{v} + (\nabla \mathbf{v})^T - \frac{2}{3} (\nabla \cdot \mathbf{v}) \mathbf{I} \right] + \zeta (\nabla \cdot \mathbf{v}) \mathbf{I}, \quad (20)$$

In this context, it is emphasised that the relative intensity between convection and diffusion is expressed as a proportion of the Péclet number (Pe), in each equation. Furthermore, the dimensionless transport coefficients reads

$$\kappa = \mu = \rho D_\eta = T^\sigma \quad (21)$$

with $\sigma = 0.7$ and $\eta \in \{F, O\}$.

Henceforth, $\text{St} := 1$, indicating that \hat{t}_c is the residence time (i.e., $\hat{t}_c := \hat{l}_c / \hat{v}_c$).

2.4. Low-Mach-number limit

Simulating flows at low Mach numbers presents a significant challenge in computational fluid dynamics (CFD) due to the large disparity between acoustic and convective time scales. In such regimes, the speed of sound exceeds the characteristic flow velocity by orders of magnitude, creating a multi-scale problem that complicates numerical modelling. This phenomenon is ubiquitous in natural systems – such as atmospheric or biological flows – and engineering applications – such as cooling and reacting flows –, for which resolving acoustic interactions alongside bulk fluid motion demands computationally intensive techniques to ensure accuracy and stability.

To address this challenge, the present section derives the low-Mach-number asymptotic limit of the conservation equations. By systematically isolating the dominant physical processes through

asymptotic analysis, the conservation equations are formally simplified to eliminate (instantaneous) acoustic effects while preserving convective and diffusive dynamics. This approach decouples the disparate scales inherent to low-Mach-number flows, yielding a simplified system that retains fidelity to the underlying physics, while enabling computationally viable simulations.

In deriving the low-Mach-number equations, a multi-scale expansion technique is employed for each dependent variable, expressed in terms of powers of the Mach number [1, 43].

Defining the fast time scale,

$$\xi := \frac{\hat{t}}{\hat{l}_c/(\hat{p}_c/\hat{\rho}_c)^{1/2}} = \frac{t}{\tilde{M}} \quad (22)$$

related to the propagation of acoustic waves, dependent variables are expanded in power series of \tilde{M} , as functions of two temporal scales (t and ξ) and one spatial scale (\mathbf{x}):

$$\mathcal{A}(\mathbf{x}, t; \tilde{M}) = \mathcal{A}_0(\mathbf{x}, t, \xi) + \tilde{M} \mathcal{A}_1(\mathbf{x}, t, \xi) + \tilde{M}^2 \mathcal{A}_2(\mathbf{x}, t, \xi) + \mathcal{O}(\tilde{M}^3), \quad (23)$$

in which $\mathcal{A} := [\rho, \mathbf{v}, p, Y_F, Y_O, T]^T$ is the state vector.

Hence, the temporal derivative consists of a flow-changing contribution ($\partial/\partial t$) and an acoustic-propagation contribution ($\tilde{M}^{-1} \partial/\partial \xi$), for a given position (\mathbf{x}) and modified Mach number (\tilde{M}). Mathematically,

$$\partial_t \mathcal{A}|_{\mathbf{x}, \tilde{M}} = \left(\frac{\partial}{\partial t} + \frac{1}{\tilde{M}} \frac{\partial}{\partial \xi} \right) \left[\mathcal{A}_0 + \tilde{M} \mathcal{A}_1 + \tilde{M}^2 \mathcal{A}_2 + \mathcal{O}(\tilde{M}^3) \right] \quad (24)$$

The derivation of the low-Mach-number equations involves substituting this expansion into the equations and integrating the first-order equations of mass, species, and energy, as well as the second-order equation of momentum, over the acoustic wave period (C_a). Note that it only captures the net acoustic effect on the average velocity field ($\overline{\mathbf{v}_0}$), within the average velocity tensor ($\overline{\mathbf{v}_0 \mathbf{v}_0} := C_a^{-1} \int_0^{C_a} \mathbf{v}_0 \mathbf{v}_0 d\xi$), as detailed in [1, 43]. Alternatively, one could have considered the acoustic spatial scale instead of the acoustic temporal scale [3].

The influence of acoustics can be completely eliminated by approximating the average velocity tensor ($\overline{\mathbf{v}_0 \mathbf{v}_0}$) as the tensor of average velocity ($\overline{\mathbf{v}_0} \overline{\mathbf{v}_0}$), culminating in the zero-Mach-number limit [44], which is equivalent to consider solely the flow time scale within the expansion [1, 5, 44, 45], viz.,

$$\mathcal{A}(\mathbf{x}, t; \tilde{M}) = \mathcal{A}_0(\mathbf{x}, t) + \tilde{M} \mathcal{A}_1(\mathbf{x}, t) + \tilde{M}^2 \mathcal{A}_2(\mathbf{x}, t) + \mathcal{O}(\tilde{M}^3). \quad (25)$$

The zero-Mach-number equations will be considered in this work. Introducing Eq. (25) into Eqs. (14) - (21), yields the following zeroth-order equations:

$$\partial_t \rho_0 + \nabla \cdot (\rho_0 \mathbf{v}_0) = 0, \quad (26)$$

$$\partial_t (\rho_0 \mathbf{v}_0) + \nabla \cdot (\rho_0 \mathbf{v}_0 \mathbf{v}_0) = -\nabla p_2 + \frac{\text{Pr}}{\text{Pe}} \nabla \cdot \boldsymbol{\tau}_0 + \frac{1}{\text{Fr}^2} (1 - \rho_0) \mathbf{e}_{x_2}, \quad (27)$$

$$\partial_t (\rho_0 Y_{F,0}) + \nabla \cdot (\rho_0 \mathbf{v}_0 Y_{F,0}) = \frac{1}{\text{Pe Le}_F} \nabla \cdot (\kappa_0 \nabla Y_{F,0}) + \text{Da} \omega_{F,0}, \quad (28)$$

$$\partial_t (\rho_0 Y_{O,0}) + \nabla \cdot (\rho_0 \mathbf{v}_0 Y_{O,0}) = \frac{1}{\text{Pe Le}_O} \nabla \cdot (\kappa_0 \nabla Y_{O,0}) + \text{Da } s \omega_{F,0}, \quad (29)$$

$$\partial_t (\rho_0 T_0) + \nabla \cdot (\rho_0 \mathbf{v}_0 T_0) = \frac{\gamma - 1}{\gamma} \frac{dp_0}{dt} + \frac{1}{\text{Pe}} \nabla \cdot (\kappa_0 \nabla T_0) - \text{Da } \Delta h^0 \omega_{F,0}, \quad (30)$$

$$p_0 = \rho_0 T_0, \quad (31)$$

in which $\kappa_0 := \kappa(T_0)$, and

$$\boldsymbol{\tau}_0 = \kappa_0 \left[\nabla \mathbf{v}_0 + (\nabla \mathbf{v}_0)^T - \frac{2}{3} (\nabla \cdot \mathbf{v}_0) \mathbf{I} \right] \quad (32)$$

Observe that, the term corresponding to the bulk viscous pressure – the second term on the right-hand side (RHS) of Eq. (20) – is not explicitly included into Eq. (32). In the low-Mach-number limit, the hydrodynamic pressure and viscous bulk pressure can be integrated, because both contribute to stresses as volumetric (isotropic) dilatations, but do not affect the energy balance or thermodynamic state. A detailed discussion can be found in [46].

The zeroth-order pressure (p_0) can be associated with the thermodynamic pressure, while the second-order one (p_2) can be associated with the hydrodynamic pressure. It is justified because they share the same order of magnitude in the momentum and state equations, respectively, as evidenced in their representation as order-unit terms.

Additionally, a constraint for p_0 emerges from the momentum equation,

$$\nabla p_0 = 0, \quad (33)$$

which implies $p_0 = p_0(t)$, i.e., the thermodynamic pressure spreads along the system instantaneously.

In the interest of clarity, only the zeroth-order index for the thermodynamic pressure (i.e., p_0) will be retained henceforward.

2.5. Flame sheet approximation

For scenarios in which the reaction rate significantly exceeds the flow-rate variation (i.e., for $\text{Da} \gg 1$), coexistence of reactants within the domain is not possible. Under the premise of comparable magnitudes between the contributions of convective and reactive terms (i.e., $\text{Da } Y_F Y_O \sim 1$), it is established that $Y_F Y_O \sim \text{Da}^{-1}$. Therefore, as Da approaches infinity, $Y_F Y_O$ tends to zero, implying that $Y_F = 0$ or $Y_O = 0$ at every point in the domain. Thus, an infinitely thin reaction zone (known as “flame sheet” or “flame surface”) separates the fuel subdomain (where $Y_F \neq 0$ and $Y_O = 0$) from the oxidiser subdomain (where $Y_F = 0$ and $Y_O \neq 0$). Meanwhile, at the flame surface, both reactants have zero concentration ($Y_F = 0$ and $Y_O = 0$).

The flame sheet approximation was initially proposed by Burke & Schumann, in a seminal paper that formalised diffusion (non-premixed) flames theory for the first time [31]. Under this Burke–Schumann limit (or kinetics), a Schvab–Zeldovich–Liñán formulation [32–36] can be employed to describe a non-equidiffusional reacting flow using coupling functions, which are transported without reaction. These functions are known as mixture fraction (Z) and excess enthalpy (H), and their equations replace species and energy equations.

By subtracting Eq. (29) multiplied by Le_O / Le_F , from Eq. (28) multiplied by S , an equation for $Z := SY_F - Y_O + 1$ is obtained as

$$\partial_t(\rho Z) + \nabla \cdot (\rho \mathbf{v} Z) = \frac{1}{Le Pe} \nabla \cdot (\kappa \nabla Z) \quad (34)$$

in which $S := s Le_O / Le_F$ is a generalised stoichiometric coefficient, and

$$Le(Z) := (Le_F - Le_O)\theta(Z - 1) + Le_O, \quad (35)$$

with θ being the Heaviside step function. Note that under this definition of mixture fraction (a rescaled version), the flame is always located on the level curve $Z = 1$.

Analogously, by adding Eq. (28) multiplied by Le_F , Eq. (29) multiplied by Le_O , and Eq. (30) multiplied by $(S + 1)/Q$, an equation for $H := (S + 1)T/Q + Y_F + Y_O$ is derived as

$$\partial_t(\rho H) + \nabla \cdot (\rho \mathbf{v} H) = \frac{S + 1}{Q} \frac{\gamma - 1}{\gamma} \frac{dp_0}{dt} + \frac{1}{Pe} [\nabla \cdot (\kappa \nabla H) + N \nabla \cdot (\kappa \nabla Z)] \quad (36)$$

in which $Q := \Delta h^0 / Le_F$ is a generalised heat released, and

$$N(Z) := (N_F - N_O)\theta(Z - 1) + N_O, \quad (37)$$

with $N_F := (1 - Le_F)/(S Le_F)$ and $N_O := (Le_O - 1)/Le_O$.

To close the system, it is missing an equation for the thermodynamic pressure (p_0) [47]. Returning the left-hand side (LHS) of Eq. (36) to primitive variables, using the equation of state (31) to identify the pressure term in LHS, taking into account the mixture fraction equation (34) and the definition of the function N in Eq. (37), one finds

$$\frac{dp_0}{dt} = \frac{\gamma}{V} \left\{ \frac{Q}{S + 1} \frac{1}{Pe} \int_V [\nabla \cdot (\kappa \nabla H) + \mathcal{N} \nabla \cdot (\kappa \nabla Z)] dV - p_0 \int_V (\nabla \cdot \mathbf{v}) dV \right\} \quad (38)$$

i.e., p_0 is obtained as solution of an ordinary differential equation, over a domain with volume V . Evidently, \mathcal{N} has the same behaviour as N ,

$$\mathcal{N}(Z) := (\mathcal{N}_F - \mathcal{N}_O)\theta(Z - 1) + \mathcal{N}_O, \quad (39)$$

but with $\mathcal{N}_F := -1/S$ and $\mathcal{N}_O := 1$.

Two simplifications are possible depending on the system boundary:

(i) for enclosed systems,

$$p_0 \int_V \frac{1}{T} dV = \int_V \rho dV = m, \quad (40)$$

i.e., p_0 can be obtained by integrating the equation of state over the domain volume (V), since the total mass (m) remains constant over time; and

(ii) for open systems,

$$p_0 = \frac{\hat{p}_0}{\hat{p}_c} = 1, \quad (41)$$

i.e., the thermodynamic pressure is determined by atmospheric pressure, as its influence is instantaneously transmitted from the boundary to the entire domain.

Therefore, the direct use of Eq. (38) is only required for semi-enclosed systems, i.e., for which the degree of openness varies over time (e.g., internal combustion engine cylinders).

2.6. Final model

Summarising, a chemically reacting flow at low Mach number, considering buoyancy effects, and under the flame surface approximation (infinitely fast chemistry), can be mathematically described by the following system of (dimensionless) equations:

$$\partial_t \rho + \nabla \cdot (\rho \mathbf{v}) = 0, \quad (42)$$

$$\partial_t (\rho \mathbf{v}) + \nabla \cdot (\rho \mathbf{v} \mathbf{v}) = -\nabla p + \frac{\text{Pr}}{\text{Pe}} \nabla \cdot \boldsymbol{\tau} + \frac{1}{\text{Fr}^2} (1 - \rho) \mathbf{e}_{x_2}, \quad (43)$$

$$\rho \partial_t Z + \rho (\mathbf{v} \cdot \nabla) Z = \frac{1}{\text{Le Pe}} \nabla \cdot (\kappa \nabla Z), \quad (44)$$

$$\rho \partial_t H + \rho (\mathbf{v} \cdot \nabla) H = \zeta d_t p_0 + \frac{1}{\text{Pe}} [\nabla \cdot (\kappa \nabla H) + \text{N} \nabla \cdot (\kappa \nabla Z)], \quad (45)$$

with $\zeta := (S + 1)(\gamma - 1)/(\gamma Q)$, $d_t p_0 := dp_0/dt$, and the viscous stress tensor ($\boldsymbol{\tau}$) modelled by the (simplified) Navier–Poisson law

$$\boldsymbol{\tau} = \kappa \left[\nabla \mathbf{v} + (\nabla \mathbf{v})^T - \frac{2}{3} (\nabla \cdot \mathbf{v}) \mathbf{I} \right], \quad (46)$$

In addition, the following piecewise definitions for the Lewis number (Le) and N account for differential diffusion:

$$\text{Le}(Z) := (\text{Le}_F - \text{Le}_O)\theta(Z - 1) + \text{Le}_O, \quad (47)$$

and

$$\text{N}(Z) := (\text{N}_F - \text{N}_O)\theta(Z - 1) + \text{N}_O. \quad (48)$$

The system is complemented by the ideal gas law

$$p_0 = \rho T, \quad (49)$$

to describe the thermodynamic state, and a power law to capture the temperature dependence of transport coefficients

$$\kappa = T^\sigma \quad (50)$$

with $\sigma = 0.7$.

The equations for mixture fraction (Z) and excess enthalpy (H) variables have been expressed in the non-divergent (or non-conservative) form for convenience. Specially, for the calculus of the

regularised temperature derivative, as described in Sec. 3.5. The modelled system is, naturally, subject to specific initial and boundary conditions, which will be described on a case-by-case basis, in Sec. 4.

Compared to related works, the proposed model additionally accounts for the effects of buoyancy and preferential or differential diffusion, in a more simplified combustion formulation.

3. Numerical Method

Hydrodynamic variables evolution relies on a fractional time-step (or projection) method [48], as proposed in [10, 49]. This method was introduced by Chorin [15] and T  mam [16], whose the former proposes an elegant interpretation based on the decomposition theorem of Ladyzhenskaya (or Helmholtz–Hodge decomposition) [48, 50]. Specifically, the fractional time-step method involves a formal separation of the pressure term from the other momentum terms, consisting, therefore, an operator splitting technique [19]. An insightful approach is to interpret this method as a block LU decomposition, as proposed by Perot [20, 21]. This perspective clarifies the underlying assumptions, addressing persistent questions about boundary conditions for intermediate (temporary) velocity and pressure fields, as well as about the degradation of the temporal accuracy. An elliptic equation for pressure enforces the velocity divergence constraint (i.e., pressure acts as a Lagrange multiplier) [20]. In general, an inhomogeneous restriction on the velocity divergence is imposed (related to thermal compressibility), which is simplified to a homogeneous one in the incompressible limit [9].

Partial differential equations are converted to a system of ordinary differential equations via spatial discretisation (method of lines) [51, 52], enabling the modular use of temporal integrators. Therefore, a predictor-corrector method is employed for time marching. The predictor stage uses a second-order Adams–Bashforth scheme [53], and incorporates a pressure correction step to ensure mass conservation. Similarly, the corrector stage is constructed under a second-order Adams–Moulton scheme [53], also involving a pressure correction step. The combination of multi-step methods, explicit for the predictor (Adams–Bashforth method) and implicit for the corrector (Adams–Moulton method), is well-established and has already been used in related studies [49, 54]. In both stages, the pressure calculation arises from the solution of a Poisson equation, as previously mentioned, representing the most significant computational demand of the method.

The physical domain is discretised into a collocated grid. The spatial discretisation of operators is based on centred approximations, along with the introduction of auxiliary fluxes to prevent non-physical pressure oscillations, known as “odd-even decoupling” [10, 55] (or “checkerboarding”), which arises from the inability of the system to conserve mass and momentum with the equivalent accuracy, when all variables are calculated at the same points.

3.1. Temporal discretisation

Superscripts are used for time indication. Known values from the past (t_{n-m}) and at the present (t_n) are indicated by indices ‘ $n - m$ ’ and ‘ n ’, respectively, in which $t_{n-m} := t_n - m\Delta t$, for an integer m and the time step Δt . Unknown, predicted and corrected values at the future $t_{n+1} := t_n + \Delta t$ are represented by indices ‘ $*$ ’ and ‘ $n + 1$ ’, in this order.

3.1.1. Predictor stage

- (i) The estimated value of the mixture fraction (Z^*) is computed using Eq. (44), from known values of instants t_n and t_{n-1} , namely

$$\frac{Z^* - Z^n}{\Delta t} = \frac{3}{2} \text{Res}_Z(\rho^n, \mathbf{v}^n, Z^n) - \frac{1}{2} \text{Res}_Z(\rho^{n-1}, \mathbf{v}^{n-1}, Z^{n-1}), \quad (51)$$

in which

$$\text{Res}_Z := \frac{1}{\rho} \left[-\rho (\mathbf{v} \cdot \nabla) Z + \frac{1}{\text{Le Pe}} \nabla \cdot (\kappa \nabla Z) \right] \quad (52)$$

- (ii) Similarly, the predicted value for the excess enthalpy (H^*) is derived from Eq. (45) as

$$\begin{aligned} \frac{H^* - H^n}{\Delta t} = & \frac{3}{2} [\text{Res}_H(\rho^n, \mathbf{v}^n, H^n) + f_H(\rho^n, d_t p_0|^n, Z^n)] - \\ & - \frac{1}{2} [\text{Res}_H(\rho^{n-1}, \mathbf{v}^{n-1}, H^{n-1}) + f_H(\rho^{n-1}, d_t p_0|^{n-1}, Z^{n-1})], \quad (53) \end{aligned}$$

in which

$$\text{Res}_H := \frac{1}{\rho} \left[-\rho (\mathbf{v} \cdot \nabla) H + \frac{1}{\text{Pe}} \nabla \cdot (\kappa \nabla H) \right], \quad (54a)$$

$$f_H := \frac{1}{\rho} \underbrace{\left[\zeta d_t p_0 + \frac{N}{\text{Pe}} \nabla \cdot (\kappa \nabla Z) \right]}_{\text{source term for } H\text{-equation}}, \quad (54b)$$

with

$$d_t p_0|^n \approx \frac{3p_0^n - 4p_0^{n-1} + p_0^{n-2}}{2\Delta t}, \quad \text{and} \quad d_t p_0|^{n-1} \approx \frac{3p_0^{n-1} - 4p_0^{n-2} + p_0^{n-3}}{2\Delta t}. \quad (55)$$

- (iii) The predicted value for temperature, $T^* = T(Z^*, H^*)$, is determined using the definitions of Z and H (see Sec. 3.5 for details). Consequently, density (ρ^*) is predicted from Eq. (49). Effectively,

$$\rho^* = \frac{p_0^*}{T^*}. \quad (56)$$

The thermodynamic pressure (p_0^*) is computed using Eqs. (38), (40) or (41), depending on the system boundary.

- (iv) At this step, the predicted value for the hydrodynamic pressure (p^*) can be computed.

The momentum equation, i.e., Eq. (43), can be semi-discretised as

$$\frac{\rho^* \mathbf{v}^* - \rho^n \mathbf{v}^n}{\Delta t} = \frac{3}{2} [\text{Res}_v(\rho^n, \mathbf{v}^n) + \mathbf{f}_v(\rho^n)] - \frac{1}{2} [\text{Res}_v(\rho^{n-1}, \mathbf{v}^{n-1}) + \mathbf{f}_v(\rho^{n-1})] - \frac{1}{\Delta t} \nabla P^*, \quad (57)$$

in which

$$\text{Res}_v := -\nabla \cdot (\rho \mathbf{v} \mathbf{v}) + \frac{\text{Pr}}{\text{Pe}} \nabla \cdot \boldsymbol{\tau}, \quad (58a)$$

$$\mathbf{f}_v := \underbrace{\frac{1}{\text{Fr}^2} (1 - \rho) \mathbf{e}_y}_{\text{source term for } v\text{-equation}} \quad (58b)$$

$$P^* := p^* \Delta t \quad (58c)$$

Taking the divergence of Eq. (57), one can get a Poisson equation for pressure, i.e.,

$$-\nabla^2 P^* = \nabla \cdot (\rho^* \mathbf{v}^*) - \nabla \cdot (\rho^* \tilde{\mathbf{v}}), \quad (59)$$

in which

$$\frac{\rho^* \tilde{\mathbf{v}}}{\Delta t} := \frac{\rho^n \mathbf{v}^n}{\Delta t} + \frac{3}{2} [\text{Res}_v(\rho^n, \mathbf{v}^n) + \mathbf{f}_v(\rho^n)] - \frac{1}{2} [\text{Res}_v(\rho^{n-1}, \mathbf{v}^{n-1}) + \mathbf{f}_v(\rho^{n-1})] \quad (60)$$

Finally, from the continuity equation, i.e., Eq. (42),

$$\nabla \cdot (\rho^* \mathbf{v}^*) = -\partial_t \rho|^* \approx -\frac{3\rho^* - 4\rho^n + \rho^{n-1}}{2\Delta t}, \quad (61)$$

In essence, this approach estimates the temporal derivative of density using backward second-order finite differences. Therefore, mass conservation is enforced via pressure.

Employing Eqs. (60) and (61), the predicted pressure value (p^*) can be determined using Eq. (59).

(v) Finally, returning to Eq. (57), a prediction for velocity (\mathbf{v}^*) can be obtained.

3.1.2. Corrector stage

(i) The mixture fraction (Z^{n+1}) at the next time step (t_{n+1}) is computed from Eq. (44), incorporating values from the predictor step (future) and the previous time step (present), namely

$$\frac{Z^{n+1} - Z^n}{\Delta t} = \frac{1}{2} \text{Res}_Z(\rho^*, \mathbf{v}^*, Z^*) + \frac{1}{2} \text{Res}_Z(\rho^n, \mathbf{v}^n, Z^n). \quad (62)$$

(ii) Analogously, the corrected value of excess enthalpy (H^{n+1}) can be derived from Eq. (45) as

$$\begin{aligned} \frac{H^{n+1} - H^n}{\Delta t} = & \frac{1}{2} [\text{Res}_H(\rho^*, \mathbf{v}^*, H^*) + f_H(\rho^*, d_t p_0|^*, Z^*)] + \\ & + \frac{1}{2} [\text{Res}_H(\rho^n, \mathbf{v}^n, H^n) + f_H(\rho^n, d_t p_0|^n, Z^n)], \end{aligned} \quad (63)$$

in which

$$d_t p_0|^* \approx \frac{3p_0^* - 4p_0^n + p_0^{n-1}}{2\Delta t}. \quad (64)$$

- (iii) The temperature, $T^{n+1} = T(Z^{n+1}, H^{n+1})$, is computed using the definitions of Z and H . From Eq. (49), the value for ρ^{n+1} is, then, obtained as

$$\rho^{n+1} = \frac{p_0^{n+1}}{T^{n+1}}, \quad (65)$$

in which p_0^{n+1} is derived from Eqs. (38), (40) or (41), as appropriated.

- (iv) The corrected pressure (p^{n+1}) is determined analogously to the predicted pressure (p^*), namely

$$\frac{\rho^{n+1}\mathbf{v}^{n+1} - \rho^n\mathbf{v}^n}{\Delta t} = \frac{1}{2} [\text{Res}_v(\rho^*, \mathbf{v}^*) + \mathbf{f}_v(\rho^*)] + \frac{1}{2} [\text{Res}_v(\rho^n, \mathbf{v}^n) + \mathbf{f}_v(\rho^n)] - \frac{1}{\Delta t} \nabla P^{n+1}, \quad (66)$$

in which P^{n+1} is the corrector-stage analogous of Eq. (58c).

Taking the divergence of Eq. (66), a Poisson equation for pressure emerges, i.e.,

$$-\nabla^2 P^{n+1} = \nabla \cdot (\rho^{n+1}\mathbf{v}^{n+1}) - \nabla \cdot (\rho^{n+1}\check{\mathbf{v}}) \quad (67)$$

in which

$$\frac{\rho^{n+1}\check{\mathbf{v}}}{\Delta t} := \frac{\rho^n\mathbf{v}^n}{\Delta t} + \frac{1}{2} [\text{Res}_v(\rho^*, \mathbf{v}^*) + \mathbf{f}_v(\rho^*)] + \frac{1}{2} [\text{Res}_v(\rho^n, \mathbf{v}^n) + \mathbf{f}_v(\rho^n)] \quad (68)$$

Finally, from the mass conservation equation (42),

$$\nabla \cdot (\rho^{n+1}\mathbf{v}^{n+1}) = -\partial_t \rho|^{n+1} \approx -\frac{3\rho^{n+1} - 4\rho^n + \rho^{n-1}}{2\Delta t}, \quad (69)$$

utilising the same approximation as the predictor stage.

Hence, using Eqs. (68) and (69), the pressure value at time t_{n+1} (i.e., p^{n+1}) can be computed from Eq. (67).

- (v) The corrected velocity (\mathbf{v}^{n+1}) is calculated from Eq. (66).

Note that multi-step (or multi-point) methods require the prescription of values for various (past) time points, which are not always available. Therefore, it is recommended to start the simulation with lower-order versions and gradually transitioning to their higher-order analogous, as the necessary data becomes available. Concretely, for this case, one starts with a first order Adams–Bashforth method (i.e., the Euler method) for the predictor. While the corrector can continue using the same second-order method. This combination is known as the Heun’s method.

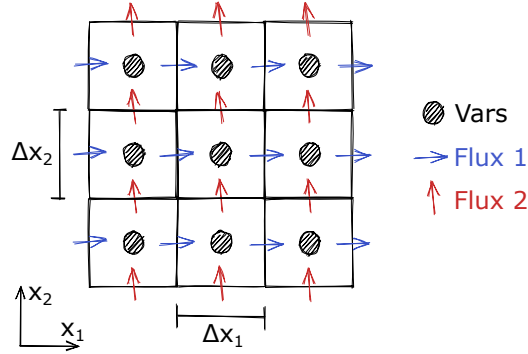


Figure 1: A collocated bidimensional grid in Cartesian coordinates, with spacing Δx_1 and Δx_2 for x_1 - and x_2 -directions, respectively. Each variable is stored at the centre of grid cells (circles), while auxiliary fluxes are defined at cell interfaces of the corresponding direction (arrows), i.e. flux 1 (F_1) for the horizontal direction (x_1), and flux 2 (F_2) for the vertical direction (x_2).

3.2. Spatial Discretisation

Basically, it is possible to discretise the physical domain into regular, staggered, or collocated grids [55]. Regular grids – where all variables are placed at the same position – provide advantages in terms of easier computational implementation, parallelisation, adaptability to curvilinear coordinates, and extension to high-order schemes. Staggered grids – where velocity components are strategically dislocated in relation to scalar variables – avoid numerical pressure oscillations due to the resulting strong “odd-even coupling” (i.e., fluxes at cell-interfaces are appropriated to enforces mass conservation locally). Collocated grids – where all variables are located at the same point, similar to regular grids, while auxiliary fluxes are conveniently defined around that point, similar to staggered grids – combining the good features of both regular and staggered grids, in principle.

This study follows the approach of [55], developed for discrete conservation of kinetics energy in incompressible flows, and extended to variable-density low-Mach-number flows, encompassing both non-reacting [47] and reacting [10] scenarios. Concretely, it employs a collocated grid in Cartesian coordinates, as illustrated in Fig. 1. The operators are discretised using a centred finite-differences scheme, with flux interpolation to avoid numerical pressure oscillations.

3.2.1. Interpolation and finite-difference operators

The interpolation and finite-difference operators are defined below. It should be noted that odd-index operators (i.e., for odd n) transfer data between central points and interfaces, while even-index operators (i.e., for even n) keep the data where it is originally defined. For example, when information is to be passed from a centroid to an interface, or from an interface to a centroid, the respective odd-index operator needs to be used. When information corresponding to a centroid or an interface must be processed in the same place, the respective even-index operator should be invoked.

Viz., the adopted interpolation operator is given by

$$\bar{\phi}^{nx_i}|_{x_i,I} := \frac{(x_{i,I} - x_{i,I-n/2})\phi(x_{i,I+n/2}) + (x_{i,I+n/2} - x_{i,I})\phi(x_{i,I-n/2})}{x_{i,I+n/2} - x_{i,I-n/2}}, \quad (70)$$

and the finite-difference operator is given by

$$\frac{\delta_n \phi}{\delta_n x_i}|_{x_i,I} := \frac{\phi(x_{i,I+n/2}) - \phi(x_{i,I-n/2})}{x_{i,I+n/2} - x_{i,I-n/2}} \quad (71)$$

both are derived from Taylor series expansion for a non-uniform grid. Note that the first index (' i ') refers to the direction (i.e., x_1 , x_2 or x_3) and the second index (' I '), to the domain partition (or grid) index, omitting constant directions. Thus, I could indicate either a cell centre or interface. They are (locally) second-order accurate, and can be combined (varying ' n ') to produce higher-order approximations.

3.2.2. Integration operator

A collocated grid (see Fig. 1) naturally induces numerical integration via a middle Riemann sum (or midpoint rule), as the value at the centroid represents the value across the entire cell.

Therefore, integrals are discretised as

$$\int_V \phi(x_1, x_2, x_3) dV \approx \sum_{I,J,K} \phi(x_{1,I}, x_{2,J}, x_{3,K}) \Delta V_{(I,J,K)} \quad (72)$$

in which $\phi(x_{1,I}, x_{2,J}, x_{3,K})$ is ϕ evaluated at the point $(x_{1,I}, x_{2,J}, x_{3,K})$, whose volume of the corresponding cell is $\Delta V_{(I,J,K)}$. The same idea applies to bidimensional and unidimensional integrals, with the overall spatial error of second order [56].

3.2.3. Discretisation strategy

The discretisation is based on the operators previously delineated, as proposed by [10, 47, 55]. Only the corrector-stage schemes will be presented herein. The schemes for the predictor stage are entirely analogous and, for the sake of brevity, will be omitted.

Auxiliary fluxes are defined at the midpoint of interfaces, necessitating the transfer of data from centroids to interfaces. Thus, odd-index operators should be utilised. Hence, from Eqs. (66) and (68), and discrete operators of Eqs. (70) and (71),

$$F_i^{n+1} := \overline{\rho^{n+1}} \bar{v}_i^{1x_i} - \frac{\delta_1 P^{n+1}}{\delta_1 x_i} \quad (73)$$

Alternatively to the derivation in Sec. 3.1, a discretisation of the pressure Poisson equation can be accomplished, directly, from the continuity equation. Starting from Eq. (69) and employing auxiliary fluxes (F_i^{n+1}) of Eq. (73), one gets

$$\partial_t \rho|^{n+1} + \frac{\delta_1 F_i^{n+1}}{\delta_1 x_i} = 0 \quad (74)$$

In addition, velocity components (v_i) can be computed from Eq. (66), using P^{n+1} calculated from Eq. (74), as

$$v_i^{n+1} = \frac{1}{\rho^{n+1}} \left(\rho^{n+1} \check{v}_i - \frac{\delta_2 P^{n+1}}{\delta_2 x_i} \right) \quad (75)$$

Note that even-index operator were used, since v_i and P are defined at the same grid. Convective terms can be derived from auxiliary fluxes, given by Eq. (73), as

$$\frac{\partial}{\partial x_j} (\rho v_i v_j) \approx \frac{\delta_1}{\delta_1 x_j} (F_j \overline{v_i^{1x_i}}), \quad (76a)$$

$$\rho v_j \frac{\partial Z}{\partial x_j} \approx F_j \frac{\delta_1 Z^{1x_j}}{\delta_1 x_j} \quad (76b)$$

with the same strategy of mixture fraction (Z) being employed for excess enthalpy (H). Odd-index operators were used for convective terms, since auxiliary fluxes and primitive variables are defined at distinct grids. This procedure culminates in strong “odd-even coupling”, between pressure (mass conservation) and velocity (momentum conservation), avoiding numerical oscillations in the pressure field, common in grids where all variables are calculated at the same points.

Lastly, it is pertinent to note that operators pertaining to diffusion phenomena are discretised using standard centred-finite differences, yielding the same order of accuracy as operators associated with convection. It is equivalent to use a composition of odd-index operators.

3.3. Poisson Equation

Physically, there are no explicit boundary conditions for pressure in the low Mach number regime, which, naturally, includes the particular case of incompressibility. In this context, pressure acts as a restriction (Lagrange multiplier) on the velocity divergence to enforce the conservation of mass [57].

Given the lack of consensus in the literature on this issue (see, for instance, [58–61]), it is recommended to avoid explicitly defining boundary conditions for pressure. When working with staggered or collocated grids with auxiliary fluxes, boundary conditions for mass fluxes are known [62, 63]. In other words, auxiliary fluxes do not need to be split, as proposed in Eq. (73). Thus, boundary conditions for pressure or intermediate velocity are not required [20, 62, 63]. Another consequence is that the compatibility condition [64] is satisfied at discrete level [65, 66] – under consistent boundary conditions –, and the existence of a solution is guaranteed. However, it results in an indeterminate system, as it implies a problem subjected to pure Neumann boundary conditions [64]: an infinite set of solutions is possible, as adding any constant to a solution results in another solution. As the low-Mach-number flows only perceive pressure gradients, any solution is sufficient, and this study employs the augmented matrix method to obtain the zero-mean solution [64, 66]. This approach also regularises the solvability condition for the linear system associated with the discretisation of the Poisson equation [67], compensating any eventual residue in the discrete compatibility condition.

The pressure solution within the domain can be extrapolated to ghost cells, enabling the computation of derivatives at points adjacent to the boundary, consistently to the procedure for interior

points. This also allows for the determination of pressure on the boundary. More specifically, a quadratic extrapolation is applied at a ghost-cell point (e.g., $I = 0$) as

$$\phi(x_{i,0}) = A\phi(x_{i,1}) + B\phi(x_{i,2}) + C\phi(x_{i,3}) \quad (77)$$

in which

$$\begin{aligned} A &:= \frac{(x_{i,2} - x_{i,0})(x_{i,3} - x_{i,0})}{(x_{i,2} - x_{i,1})(x_{i,3} - x_{i,1})}, \\ B &:= \frac{(x_{i,1} - x_{i,0})(x_{i,3} - x_{i,0})}{(x_{i,1} - x_{i,2})(x_{i,3} - x_{i,2})}, \\ C &:= \frac{(x_{i,1} - x_{i,0})(x_{i,2} - x_{i,0})}{(x_{i,1} - x_{i,3})(x_{i,2} - x_{i,3})}. \end{aligned} \quad (78)$$

Note that this approach is equivalent to consider one-sided (second-order) finite differences for pressure derivatives at first-interior points.

3.4. Immersed Boundary Method

The immersed boundary method (IBM), firstly presented by Peskin [22], provides an ingenious technique for modelling intricate fluid dynamics, initially applied to circulatory system modelling of flows around heart valves. This method represents a notable advancement in computational fluid dynamics, enabling the description of complex flow-structure interactions using orthogonal coordinates on non-conforming grids.

The original proposal of Peskin involves augmenting the (incompressible) momentum equation with a forcing term to account for the presence of an immersed body within the flow, which is, precisely, the essence of this method [23]. In fact, a volumetric forcing term (\mathbf{F}_v) can be added to Eq. (43), resulting in

$$\partial_t(\rho\mathbf{v}) + \nabla \cdot (\rho\mathbf{v}\mathbf{v}) = -\nabla p + \frac{\text{Pr}}{\text{Pe}} \nabla \cdot \boldsymbol{\tau} + \frac{1}{\text{Fr}^2}(1 - \rho)\mathbf{e}_{x_2} + \mathbf{F}_v, \quad (79)$$

with $\mathbf{F}_v = \mathbf{F}_v(\mathbf{x}, t)$ adjusted dynamically to represent the response forces, related to the presence of an immersed body. The specific form of \mathbf{F}_v depends on the particular method, with several possibilities [24, 25].

An elegant idea is to consider a solid obstacle as a porous medium of negligible permeability (\hat{K} [length²]), i.e., $0 < \hat{K} \ll 1$. This approach was proposed originally by Arquis [28], subsequently known as the penalisation (or penalty) method. Because of the physical motivation, as well as the mathematical robustness [37, 38], the present study adopts a penalisation method, which implies the following forcing term definition

$$\mathbf{F}_v := -\chi \frac{\text{Pr}}{\text{Pe Da}_{ib}} \kappa (\mathbf{v} - \mathbf{v}_{ib}) \quad (80)$$

in which $\chi = \chi(\mathbf{x}, t)$ is a characteristic (or mask) function, $\text{Da}_{ib} := \hat{K}_{ib}/\hat{l}_c^2 \ll 1$ is the immersed-boundary (IB) Darcy number – associated with the imposed permeability \hat{K}_{ib} – and the velocity

\mathbf{v}_{ib} . Physically, \mathbf{F}_v represents a linear momentum sink (or a linear damping force), inversely proportional to Da_{ib} , acting against the difference $\mathbf{v} - \mathbf{v}_{ib}$. In the context of IBM, it is known as the penalisation (or penalty) term. A relevant observation is that, the work done by this damping force scales with \tilde{M}^2 , and does not contribute to the enthalpy in the low-Mach-number equations (see Sec. 2.4).

The parameter Da_{ib} is critical, as it controls the proper convergence to the actual solution, on the one hand, and the integration stability, on the other, requiring a compromise between correct imposition ($\text{Da}_{ib} \rightarrow 0$), and relaxation of the time-step restriction ($\text{Da}_{ib} \rightarrow 1$). Indeed, it imposed the stability condition $\Delta t \leq c(\text{Re Da}_{ib})$ – for a real, scheme-dependent constant c –, when using an explicit method. The characteristic function (χ) is commonly related to a discrete version of the Heaviside step function – defined as 0, for a fluid point, and as 1, for an IB point. The present formulation considers the shifted characteristic function derived by Iwakami [26]. The basic idea is to extend the body over the fluid by $(\text{Da}_{ib})^{1/2}$, which corresponds to the (dimensionless) Brinkman layer thickness (or Brinkman screening length), a transition zone connecting the fluid and porous medium behaviours. This approach categorically reduces the error in the fluid region, after the transition layer. The physical justification of this method efficacy appears to stem from the appropriate representation of the solid dimensions – i.e., the “effective length” is a proper representation of the body length – because the transition layer is transferred from the porous-medium interior to the fluid region. Mathematically, the wavenumbers associated with the penalised-numerical solution coincide with those related to the actual solution in the fluid region (except into the Brinkman layer), as shown in [26]. Naturally, the grid resolution should be suffice to capture the transition zone (i.e., $\Delta x_i \lesssim (\text{Da}_{ib})^{1/2}$ for $i = 1, 2, 3$).

Analogously to the momentum forcing, the imposition of boundary conditions on the immersed body can be consistently accomplished – for mixture fraction (F_Z) and excess enthalpy (F_H), respectively – defining the penalisation terms

$$F_Z := -\chi \frac{1}{\text{Le Pe Da}_{ib}} \kappa (Z - Z_{ib}) \quad (81)$$

and

$$F_H := -\chi \frac{1}{\text{Pe Da}_{ib}} \kappa (H - H_{ib}), \quad (82)$$

in which Z_{ib} and H_{ib} are the respective conditions for Z and H on the body surface.

Penalisation terms are discretised using the same second-order scheme as described for other forcing terms in Sec. 3. Additionally, for the case of mass ejection from the body, a mass source term, $S_m = S_m(t, \mathbf{x})$, must be added to the continuity equation, in consonance with the imposed velocity. Namely,

$$\partial_t \rho + \nabla \cdot (\rho \mathbf{v}) = S_m \quad (83)$$

which will be, actually, accounted for into the forcing term of the pressure Poisson equation.

This penalisation method follows a dimensionally consistent derivations of forcing terms, because *a mathematical model for physical systems should always incorporate physically consistent terms. Even for purely numerical purposes, terms inherently carry physical meaning.* Neglecting this principle makes interpreting results difficult or, worse, may lead to simulation divergence or non-physical solutions.

3.5. Flame Regularisation

Although formally simplified, an infinitely thin flame implies a discontinuity of properties between the two sides (fuel and oxidiser subdomains) of the flame surface. Especially critical for finite differences (strong form), discontinuities should lead to numerical oscillations during the time-march process and may also hinder post-processing or utilisation as a base flow for additional analyses (e.g., stability analyses). This is because, the basis of finite difference methods is the Taylor series expansion, which requires functions to be infinitely differentiable and, therefore, continuous at the point of expansion.

To circumvent this issue, a regularisation technique is applied to the Heaviside function (θ), which originally models the behaviour of these properties. This method entails utilising a regularised variant of the Heaviside function (θ_ε) to achieve smooth property transitions over a thickness ε , between the fuel and oxidant subdomains, adjacent to the flame. Concretely, it involves the using of [68]

$$\theta_\varepsilon(Z - Z_{st}) := \frac{1 + \tanh[k(Z - Z_{st})]}{2} \quad (84)$$

which acts around $Z_{st} = 1$ (i.e. around the stoichiometric-mixture level, representing the flame), continuously linking properties from either flame side.

The regularisation parameter k controls the effective support. By determining a proper value for $k := [1/(2\varepsilon)] \ln[(1 - tol)/tol]$, such that it converges to θ , within a specified tolerance (tol), when $Z = \pm\varepsilon$. An appropriate choice for tol is based on the spatial truncation errors.

Hence, the regularised coefficients Le_ε , N_ε and \mathcal{N}_ε read

$$Le_\varepsilon(Z) = (Le_F - Le_O)\theta_\varepsilon(Z - 1) + Le_O \quad (85a)$$

$$N_\varepsilon(Z) = (N_F - N_O)\theta_\varepsilon(Z - 1) + N_O \quad (85b)$$

$$\mathcal{N}_\varepsilon(Z) = (\mathcal{N}_F - \mathcal{N}_O)\theta_\varepsilon(Z - 1) + \mathcal{N}_O \quad (85c)$$

Besides these three coefficients, temperature derivatives are also discontinuous at the flame. The following procedure may be adopted to circumvent this issue:

- (i) Use the definition of H and Z to write $T = T(Z, H)$, i.e.,

$$T = \frac{Q}{S+1} [F + H] \quad (86)$$

in which $F = F(Z)$ is defined by

$$F(Z) := \begin{cases} (1 - Z)/S, & \text{for } Z > 1 \\ (Z - 1), & \text{for } Z \leq 1 \end{cases} \quad (87)$$

- (ii) Identify that the discontinuity is in the derivative of F

$$F'(Z) = \begin{cases} -1/S, & \text{for } Z > 1 \\ 1, & \text{for } Z \leq 1 \end{cases} \quad (88)$$

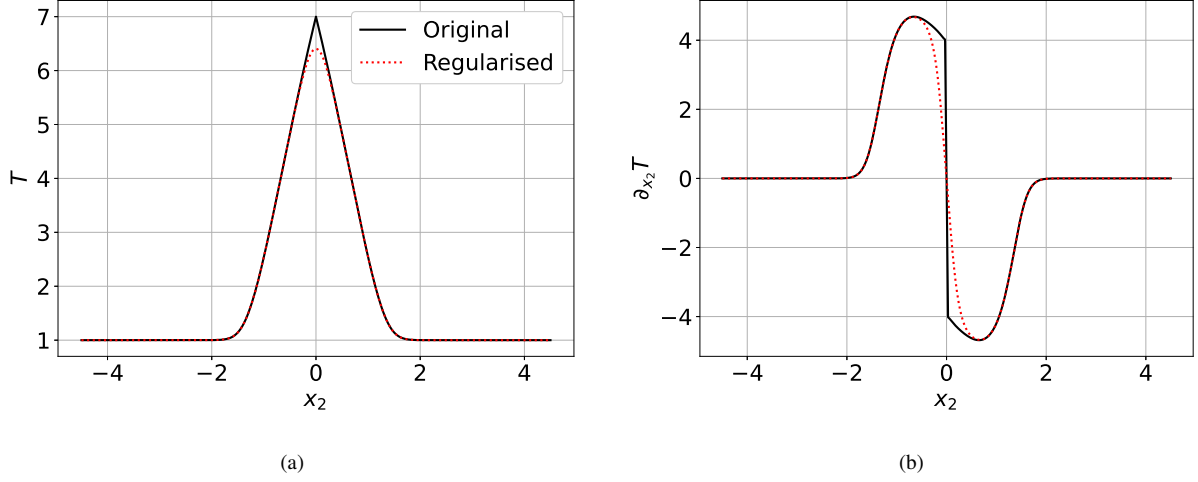


Figure 2: Comparison of original and regularised temperature (a) and temperature derivative flame-crossed profiles for a planar counterflow diffusion flame.

and, thus, apply the regularisation to it:

$$F'(Z) = (-1/S - 1) \theta_\varepsilon(Z - 1) + 1 \quad (89)$$

So, the regularised F can be recovered by integration, i.e.,

$$F_\varepsilon(Z) = \int_1^Z [-(1/S + 1) \theta_\varepsilon(z - 1) + 1] dz \quad (90)$$

or, explicitly,

$$F_\varepsilon(Z) = \frac{1}{2S} \left[-(S + 1) \frac{\ln\{\cosh[k(Z - 1)]\}}{k} + (S - 1)(Z - 1) \right]. \quad (91)$$

Note that it imposes the correct slopes for F_ε from the flame position, but does not guarantee the right level, which varies with the thickness ε . To adjust the level, F_ε must be translated to satisfy the values at the boundary, which implies a smaller maximum temperature, naturally.

Therefore, the regularised temperature (T_ε) can be expressed as

$$T_\varepsilon = \frac{Q}{S + 1} [F_\varepsilon + H] \quad (92)$$

Figure 2 shows a comparison between original and regularised profiles of temperature and its variations, along the normal direction to a planar counterflow diffusion flame. In what follows, the index ' ε ' in the regularised properties shall be omitted, for the sake of notation simplicity.

3.6. Boundary conditions

Boundary conditions are implemented using a ghost-cell method, derived from operators in Sec. 3.2.1. For instance, to impose a condition $\Phi = \Phi(x_i, t)$ at the left boundary ($I = 1/2$), the proper value for the ghost-cell $\phi(x_{i,0})$ can be set as follows:

For a Dirichlet condition.

$$\phi(x_{i,0}) = 2\Phi - \phi(x_{i,1}), \quad (93)$$

which admits the same spacing among the ghost and first interior points (i.e., a mirrored ghost-cell).

For a Neumann condition.

$$\phi(x_{i,0}) = -(x_{i,1} - x_{i,0})\Phi + \phi(x_{i,1}) \quad (94)$$

For a periodic condition.

$$\phi(x_{i,0}) = \phi(x_{i,N_{x_1}-1}) \quad (95)$$

in which N_{x_i} is the last index in the i -direction partition, also representing a ghost-cell.

For an extrapolation condition.

$$\phi(x_{i,0}) = A\phi(x_{i,1}) + B\phi(x_{i,2}) + C\phi(x_{i,3}) \quad (96)$$

with the same coefficients such as defined in Eq. (78).

3.7. Computational Implementation

The numerical model is computationally implemented in Fortran 90, procedurally, for sequential execution. The pressure Poisson equation is solved via MUMPS [69], for robustness and efficiency, a public domain parallel sparse direct solver, which implements a multifrontal method to solve large linear systems [70]. The post-processing is carried out in Python 3.

4. Numerical Experiments

For the purposes of this work, 3D cases should only add unnecessary complexity. Therefore, this section concentrates on 2D test-case simulations for constant (incompressible) and variable density flows, at low Mach numbers, with and without chemical reactions (combustion). These numerical experiments were carefully selected to check different aspects of the proposed numerical method, highlighting both its capacities and limitations. For consistency, post-processing employs discrete operators (for differentiation, interpolation, integration, etc.) with an accuracy equivalent (or greater) to that of the proposed method. This approach mitigates the introduction of additional errors.

4.1. Preliminaries

The order of convergence (b) is given by [71]

$$b = \frac{\ln(E_m/E_{m+1})}{\ln(\delta)} \quad (97)$$

in which E_m is the absolute (scalar) or a norm (vector) error for the grid with index m , and δ is the refinement ratio from the coarser (m) to the finer ($m + 1$) grid. Alternatively, for a constant refinement ratio, the order of convergence can be directly estimated using solutions (f) for three levels ($m, m + 1$ and $m + 2$) of refinement, without the necessity of an exact solution. In fact,

$$b = \ln\left(\frac{f_m - f_{m+1}}{f_{m+1} - f_{m+2}}\right) / \ln(\delta) \quad (98)$$

from Richardson extrapolations.

The grid convergence index (GCI), for the finer grid, has the form

$$\text{GCI} := F_s \frac{|\epsilon|}{\delta^a - 1} \quad (99)$$

in which $\epsilon := (f_m - f_{m+1})/f_{m+1}$ and F_s is a ‘‘safe factor’’, considered here as 1.25.

For the first two, incompressible cases, the diffusion-term coefficient is rewritten explicitly as the reciprocal of the Reynolds number, i.e., $\text{Re} := \text{Pe} / \text{Pr}$ is used. This reformulation permits a straightforward physical interpretation, since there is no thermal energy flux under constant-density scenario.

In tables and other mentions, values are presented with few decimal places, by space limitation; however, the calculations were always performed in double precision.

4.2. Taylor–Green vortex

This configuration is proposed to verify the accuracy of the hydrodynamical-variables integration. It also enables a discussion on the fractional-time step (or projection) method, with concepts commonly misunderstood.

Consider a transient, incompressible flow defined in a dimensional periodic-square domain $[0, 2\pi]^2$. Taylor–Green vortices were proposed as an analytical tool to study the laminar-turbulent transition [72]. Indeed, a closed-form solution exists for the laminar regime:

$$v_1(x_1, x_2, t) = \sin(2\pi x_1) \cos(2\pi x_2) \exp\left(-\frac{8\pi^2}{\text{Re}}t\right), \quad (100)$$

$$v_2(x_1, x_2, t) = -\cos(2\pi x_1) \sin(2\pi x_2) \exp\left(-\frac{8\pi^2}{\text{Re}}t\right), \quad (101)$$

$$p(x_1, x_2, t) = \frac{1}{4} [\cos(4\pi x_1) + \cos(4\pi x_2)] \exp\left(-\frac{16\pi^2}{\text{Re}}t\right), \quad (102)$$

given in terms of dimensionless velocity components and pressure. The characteristic values are based on the initial state, i.e., $\hat{L}_c := 2\pi$ m (the vortex wave-length), $\hat{v}_c := 1$ m/s (maximum initial velocity component), $\hat{t}_c := \hat{L}_c/\hat{v}_c$ and $\hat{p}_c := \hat{\rho}_c \hat{v}_c^2$, for a given $\hat{\rho}_c$.

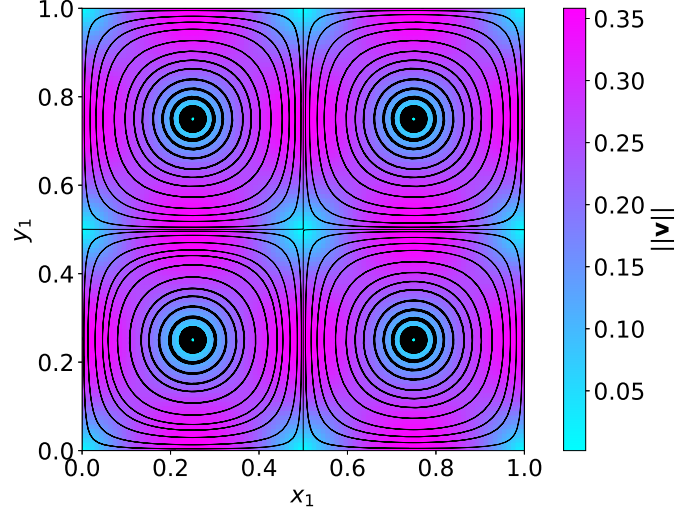


Figure 3: Streamlines of Taylor–Green vortices at $t \approx 1.3$. Light (dark) tones indicate low (high) local speeds.

In what follows, numerical and analytical results are compared at $t_{ref} = \text{Re} / (8\pi^2) \approx 1.3$ for $\text{Re} = 100$, which is the characteristic decay-time for velocity, related to viscous effects. After that time interval, the velocity magnitude is reduced by a factor of e^{-1} , as depicted in Fig. 3. For the pressure field, the viscous decaying is twice faster.

Boundary conditions. Periodic for the complete boundary.

Initial condition. Given by the exact solution at $t = 0$.

4.2.1. Spatial Accuracy

In consonance with the previous discussion, the theoretical convergence rate (second order) are achieved for all variables, as the solutions enter the asymptotic convergence regime, starting from the 80×80 grid resolution, as shown in Tab. 1. In addition, the symmetries of the flow are clearly present in the errors of horizontal (v_1) and vertical (v_2) components of the velocity, as expected, culminating in very close errors.

Furthermore, the most interesting aspect of this analysis is the pressure (p) behaviour, as previously underlined. To show that, values of Δt were carefully selected. Notably, for the most refined grids, the pressure convergence order deteriorates for the largest time-step, because temporal errors accumulates with spatial errors, insofar as $\Delta t \sim (\Delta x)^2$. The theoretical order is restored with Δt reduction, as spatial errors become dominant. To emphasize this distinction, the time-averaged pressure (\bar{p}), over the interval $[t - \Delta t, t]$, is also analysed:

$$\bar{p}(x_1, x_2, t) = \frac{\exp(\alpha\Delta t) - 1}{\alpha\Delta t} p \quad (103)$$

in which $\alpha := 16\pi^2 / \text{Re}$. Unlike the instantaneous pressure, \bar{p} consistently adheres to the theoretical convergence order, even for the largest time-step, as exhibit in Tab. 1.

Table 1: Spatial convergence analysis.

Var.	Step Type	Grid Resolution (Error $\times 10^m$ & Order)															
		10 \times 10		20 \times 20		40 \times 40		80 \times 80		160 \times 160		320 \times 320		640 \times 640			
		L2	L ∞	L2	L ∞	L2	L ∞	L2	L ∞	L2	L ∞	L2	L ∞	L2	L ∞		
v_1	Δt_1	Error	4.885 49	8.141 44	7.518 57	1.533 52	1.871 03	3.737 76	4.669 22	9.348 00	1.166 68	2.338 34	2.916 27	5.846 60	7.290 24	1.461 68	
		Order	–	–	2.70	2.41	2.01	2.04	2.00	2.00	2.00	2.00	2.00	2.00	2.00	2.00	
	Δt_2	Error	4.901 25	8.193 13	7.617 25	1.550 24	1.893 38	3.774 11	4.723 48	9.433 87	1.180 22	2.360 12	2.950 13	5.901 27	7.375 07	1.475 57	
		Order	–	–	2.69	2.40	2.01	2.04	2.00	2.00	2.00	2.00	2.00	2.00	2.00	2.00	
	Δt_3	Error	4.902 85	8.198 31	7.627 17	1.551 92	1.895 65	3.777 75	4.728 93	9.444 96	1.181 57	2.362 31	2.953 52	5.906 87	7.383 56	1.478 02	
		Order	–	–	2.68	2.40	2.01	2.04	2.00	2.00	2.00	2.00	2.00	2.00	2.00	2.00	
	v_2	Δt_1	Error	4.742 95	8.595 83	7.518 52	1.527 49	1.871 03	3.735 97	4.669 22	9.347 74	1.166 68	2.338 34	2.916 27	5.846 60	7.290 24	1.461 68
			Order	–	–	2.66	2.49	2.01	2.03	2.00	2.00	2.00	2.00	2.00	2.00	2.00	2.00
		Δt_2	Error	4.759 61	8.653 99	7.617 22	1.545 62	1.893 38	3.773 73	4.723 48	9.435 77	1.180 22	2.360 12	2.950 13	5.901 27	7.375 07	1.475 57
			Order	–	–	2.64	2.49	2.01	2.03	2.00	2.00	2.00	2.00	2.00	2.00	2.00	2.00
		Δt_3	Error	4.761 30	8.659 81	7.627 14	1.547 44	1.895 65	3.777 56	4.728 93	9.444 94	1.181 57	2.362 31	2.953 52	5.906 87	7.383 56	1.478 02
			Order	–	–	2.64	2.48	2.01	2.03	2.00	2.00	2.00	2.00	2.00	2.00	2.00	2.00
p		Δt_1	Error	7.248 61	16.7021	1.152 42	2.711 54	2.677 62	5.525 58	6.754 80	1.358 42	1.782 06	3.564 74	5.403 99	1.081 25	2.301 11	4.603 59
			Order	–	–	2.65	2.62	2.11	2.29	1.99	2.02	1.92	1.93	1.72	1.72	1.23	1.23
		Δt_2	Error	7.262 72	16.7617	1.158 69	2.740 32	2.682 47	5.636 97	6.664 19	1.344 27	1.673 44	3.352 41	4.277 11	8.556 03	1.164 19	2.328 69
			Order	–	–	2.65	2.61	2.11	2.28	1.99	2.07	1.97	2.00	1.88	1.97	1.88	1.88
		Δt_3	Error	7.264 13	16.7676	1.159 33	2.743 27	2.683 55	5.661 60	6.656 46	1.348 71	1.662 61	3.332 43	4.164 43	8.333 18	1.050 50	2.103 69
			Order	–	–	2.65	2.61	2.11	2.28	2.00	2.07	1.99	2.02	2.00	2.00	1.99	2.00
	p	Δt_1	Error	7.248 16	16.6996	1.151 28	2.709 13	2.665 01	5.503 00	6.628 12	1.333 78	1.655 36	3.312 40	4.137 04	8.279 12	1.034 17	2.069 82
			Order	–	–	2.65	2.62	2.11	2.30	2.01	2.04	2.00	2.01	2.00	2.00	2.00	2.00
		Δt_2	Error	7.262 67	16.7614	1.158 57	2.740 08	2.681 21	5.634 46	6.651 53	1.341 81	1.660 77	3.327 24	4.150 42	8.303 09	1.037 50	2.075 41
			Order	–	–	2.65	2.61	2.11	2.28	2.01	2.07	2.00	2.01	2.00	2.00	2.00	2.00
		Δt_3	Error	7.264 13	16.7676	1.159 32	2.743 24	2.683 42	5.661 35	6.655 19	1.348 46	1.661 34	3.329 91	4.151 75	8.307 86	1.037 82	2.078 34
			Order	–	–	2.65	2.61	2.11	2.28	2.00	2.07	2.00	2.02	2.00	2.00	2.00	2.00

Notes:

- Errors scaled by 10^{-m} , in which m corresponds to grid sizes:
 - 10×10 : $m = 3$; 20×20 : $m = 4$; 40×40 : $m = 5$; 80×80 : $m = 6$;
 - 160×160 : $m = 7$; 320×320 : $m = 8$; 640×640 : $m = 9$.
- For p and \bar{p} , $m = 2$ for L_∞ error at 10×10 .
- Temporal steps: $\Delta t_1 = 5 \times 10^{-5}$, $\Delta t_2 = 5 \times 10^{-6}$, $\Delta t_3 = 5 \times 10^{-7}$.

A conclusion is that the discrete pressure is unconditionally first-order time accurate, requiring some clarification: the pressure in the projection method is not an “instantaneous variable”. Instead, as stated before, it arises as a constraint (Lagrangian multiplier), enforcing consistency with the continuity equation over an interval of size Δt , effectively behaving as a time-averaged pressure over this interval. By the mean value theorem, this introduces an error of $\mathcal{O}(\Delta t)$, when it is interpreted as an instantaneous value, for a specific time.

If the discrete pressure should be instantaneously described with accuracy of second order, one could refer to the modifications proposed in [73].

4.2.2. Temporal Accuracy

Isolating temporal errors in explicit (or semi-explicit) methods is generally unviable. Spatial errors dominate, and are coupled to temporal errors through stability conditions, such as the CFL constraint: $\Delta t \leq C(\Delta x)^2$, for a real, method-specific constant C .

A potential workaround involves statistical error modelling: parameterising the error (E) – e.g., $E = C_t(\Delta t)^{p_t} + C_x(\Delta x)^{p_x} + C_y(\Delta y)^{p_y}$, for real coefficients (C_t, C_x, C_y) and powers (p_t, p_x, p_y) –, constructing a balanced set of simulations across spatial and temporal resolutions, and performing non-linear regression to disentangle temporal and spatial contributions. However, this requires extensive simulations.

The present approach circumvents this challenge by leveraging predictor-corrector temporal integration. The local truncation error is quantified using the L^2 -norm of the instantaneous difference between predicted and corrected solutions. The L^2 -norm acts as a high-order spatial error filter, contributing to the isolation of temporal errors. While temporal averaging (a low-pass filter in time) could suppress high-frequency temporal artifacts, linked to spatial discretisation errors, it was unnecessary here.

Table 2 synthesises the results of temporal analysis. Time steps are selected based on grid resolution as $(\Delta t_1, \Delta t_2, \Delta t_3, \Delta t_4) = 10^{-3} \cdot (4, 2, 1, 0.5); 10^{-3} \cdot (2, 1, 0.5, 0.25); 10^{-4} \cdot (4, 2, 1, 0.5); 10^{-4} \cdot (1, 0.5, 0.25, 0.125)$, from the coarser to finer grids, respectively. Note, once again, the expected equivalence of the errors for the vertical and horizontal velocity components, originated in the flow symmetry. All variables exhibit a third-order local truncation error, consistent with the expected (globally) second-order temporal accuracy of the method [51]. The global accuracy is degraded by one order, due to error accumulation during temporal marching, which scales as $(t_{total}/\Delta t)(\Delta t)^3 \sim (\Delta t)^2$, in which t_{total} is the simulation final time.

Observe that, this analysis does not rely on access to an exact reference solution. Instead, it estimates local error by calculating the discrepancy between predicted and corrected variable values – quantities that are inherently computed at each time step. This error estimation strategy can also be used to dynamically adjust the time-step size in adaptive time-stepping methods.

The error order should be greater than the precision of the floating-point system (double-precision herein). The grid with higher resolution (400×400) is selected to show this limitation. For the case Δt_4 , discretisation errors exceeds the machine precision, producing an artificially degraded convergence order.

Table 2: Temporal convergence analysis.

Grid	Var.	Error				Local Order		
		Δt_1	Δt_2	Δt_3	Δt_4	$\Delta t_{1 \rightarrow 2}$	$\Delta t_{2 \rightarrow 3}$	$\Delta t_{3 \rightarrow 4}$
50×50	p	2.546×10^{-9}	3.173×10^{-10}	3.960×10^{-11}	4.946×10^{-12}	3.00	3.00	3.00
	v_1	2.858×10^{-9}	3.562×10^{-10}	4.445×10^{-11}	5.552×10^{-12}	3.00	3.00	3.00
	v_2	2.858×10^{-9}	3.562×10^{-10}	4.445×10^{-11}	5.552×10^{-12}	3.00	3.00	3.00
100×100	p	3.202×10^{-10}	3.996×10^{-11}	4.991×10^{-12}	6.236×10^{-13}	3.00	3.00	3.00
	v_1	3.537×10^{-10}	4.415×10^{-11}	5.516×10^{-12}	6.892×10^{-13}	3.00	3.00	3.00
	v_2	3.537×10^{-10}	4.415×10^{-11}	5.516×10^{-12}	6.892×10^{-13}	3.00	3.00	3.00
200×200	p	2.561×10^{-12}	3.200×10^{-13}	3.999×10^{-14}	4.998×10^{-15}	3.00	3.00	3.00
	v_1	2.823×10^{-12}	3.528×10^{-13}	4.409×10^{-14}	5.511×10^{-15}	3.00	3.00	3.00
	v_2	2.823×10^{-12}	3.528×10^{-13}	4.409×10^{-14}	5.511×10^{-15}	3.00	3.00	3.00
400×400	p	4.001×10^{-14}	5.001×10^{-15}	6.251×10^{-16}	7.831×10^{-17}	3.00	3.00	3.00
	v_1	4.409×10^{-14}	5.512×10^{-15}	6.894×10^{-16}	8.683×10^{-17}	3.00	3.00	2.99
	v_2	4.410×10^{-14}	5.511×10^{-15}	6.894×10^{-16}	9.126×10^{-17}	3.00	3.00	2.92

Notes: The error is based on L_2 norm of functions at the instant $t = 1.3$; *Local order* refers to the local truncation order of the temporal discretisation method.

4.3. Taylor–Couette flow

This problem is selected as a virtual laboratory to test the immersed boundary method (IBM). Since, it also admits an exact solution for comparison.

Consider the flow between two concentric cylinders, with inner radius \hat{R}_1 (rotating at angular velocity ω_1) and outer radius \hat{R}_2 (stationary, $\omega_2 = 0$). An illustration is provided in Fig. 4.

The dimensionless variables are given by:

$$r := \frac{\hat{r}}{\hat{d}} \quad \text{and} \quad v_\theta := \frac{\hat{v}_\theta}{\hat{\omega}_1 \hat{R}_1}, \quad \text{for} \quad \hat{R}_1 \leq \hat{r} \leq \hat{R}_2 \quad (104)$$

in which $\hat{d} := \hat{R}_2 - \hat{R}_1$ is the annular gap, and \hat{v}_θ is the azimuthal velocity.

The general solution for the dimensionless azimuthal velocity (v_θ) is given by:

$$v_\theta(r) = \frac{\eta}{1 - \eta^2} \left[\frac{1}{r(1 - \eta)} - r(1 - \eta) \right], \quad (105)$$

expressed in terms of the radii ratio, $\eta := \hat{R}_1 / \hat{R}_2$.

Taking $\eta = \frac{1}{2}$ ($\hat{R}_2 = 2\hat{R}_1$ and $\hat{d} = \hat{R}_1$),

$$v_\theta(r) = \frac{4 - r^2}{3r} \quad \text{for} \quad 1 \leq r \leq 2$$

which, in Cartesian coordinates, reads

$$\mathbf{v}(x_1, x_2) = \frac{1}{3} \left(\frac{4}{x_1^2 + x_2^2} - 1 \right) \begin{bmatrix} -x_2 \\ x_1 \end{bmatrix} \quad \text{for} \quad 1 \leq (x_1^2 + x_2^2) \leq 4$$

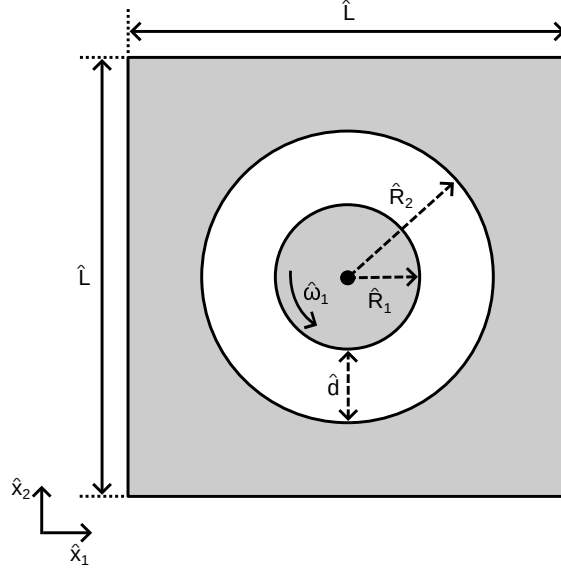


Figure 4: Axisymmetric representation of a Taylor–Couette flow.

Boundary conditions. Periodic for the complete boundary, to avoid artificial interferences.

Initial condition. Given by the exact solution.

4.3.1. Accuracy of penalised solutions

Penalised solutions for different immersed-boundary (IB) Darcy numbers ($Da_{ib} = 10^{-1}$, 10^{-2} and 10^{-3}), using the shifted characteristic (or mask) function, are compared with the exact solution, a nearest-point implementation of the direct-forcing method [74], and a penalised solution for much smaller IB Darcy number ($Da_{ib} = 10^{-6}$), using the original mask function, for reference. In addition, a grid convergence study is also explored for cases using shifted and original mask functions.

The finds are concisely presented in Fig. 5, for $Re = 1$: Figure 5a depicts a comparison for the azimuthal velocity at $\theta = \pi/4$, to test both velocity components (v_i for $i = 1, 2$); Figure 5b, in turn, synthesises a grid convergence study for penalised solutions. Concretely, the absolute error is based on the L^2 -norm of differences between exact and numerical solutions for the velocity component v_2 , in the complete annular section (i.e., for each $\theta \in [0, 2\pi]$). Errors for the v_1 -component are near identical (due to the symmetry). The results for $Re = 10$ are visually indistinguishable from those for $Re = 1$, making their presentation redundant.

The penalised solutions using the shifted mask function (i.e., the extension of the solid-to-fluid frontier) are the best descriptions of the exact solution – for $Da_{ib} = 10^{-2}$ and $Da_{ib} = 10^{-3}$ –, except into the respective transition zones, delimited in Fig. 5a by dotted vertical lines. On the other hand, the pensalised solution using the original mask function (solid vertical lines in Fig. 5a), even for a several orders of magnitude smaller IB Darcy number (i.e., $Da_{ib} = 10^{-6}$), was not able to overcome the accuracy of the shifted-mask-function solutions. This fact is due to its penalisation error [37, 38], evidenced by the saturation of dashed curves in Fig. 5b, as the penalisation error becomes dominant over the spatial discretisation error, due to the grid refinement.

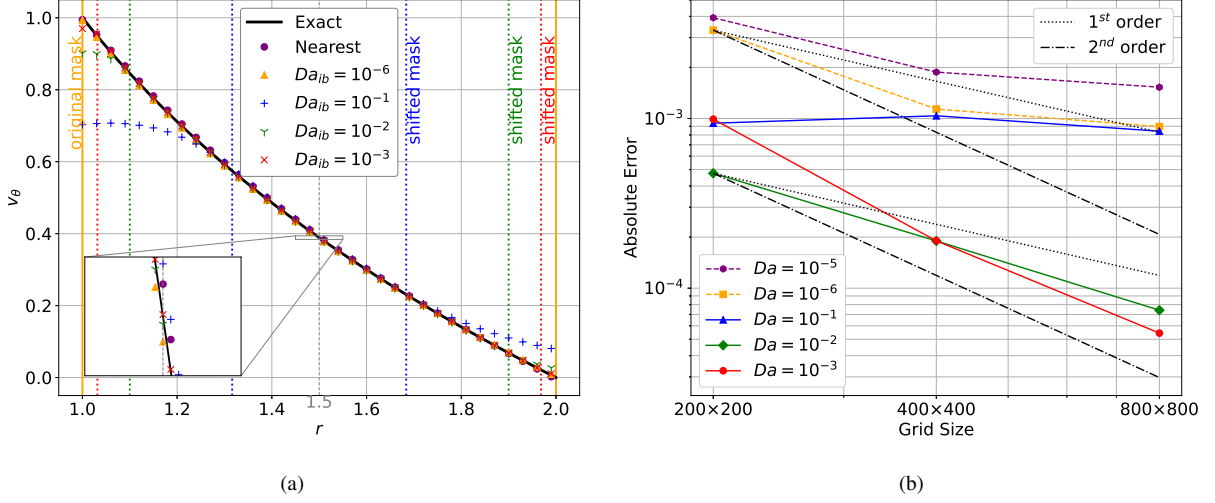


Figure 5: Comparison of penalised solutions accuracy (a) and order of convergence (b) for $Re = 1$. The behaviours under $Re = 10$ are practically indistinguishable from those presented, and have therefore been omitted for clarity.

The penalised solutions using the shifted characteristic function exhibit error reduction and improved order of convergence, as Da_{ib} increases, according to Fig. 5b. While $Da_{ib} = 10^{-3}$ attains, asymptotically, second-order convergence under grid refinement (the first grid resolution is not sufficient to capture the transition zone properly), $Da_{ib} = 10^{-2}$ displays intermediate convergence (between first and second order). For $Da_{ib} = 10^{-1}$, errors saturate at $\mathcal{O}(10^{-3})$, revealing forcing-term rigidity deficiencies – i.e., the porous medium becomes too permissive. This behaviour suggests an optimal Da_{ib} : the smallest one recovering the theoretical spatial-convergence rate, while minimally constraining grid refinement, since the condition $\Delta x_i < Da_{ib}^{1/2}$ should be satisfied along the extended solid region. Nevertheless, a formal consolidation of this optimum is deferred to future work.

It is also pertinent to mention, within the context of IBMs, that the direct forcing technique described in [75] – with transfer of properties between Lagrangian and Eulerian locations –, demonstrated pronounced numerical instability when integrated with the present method. This instability manifested, apparently, acute sensitivity to outflow conditions in the body region. For a flow around a cylinder, an outlet sponge layer offered only partial remediation. Dedicated research is needed to complete understand this issue.

4.4. Thermally driven cavity

Thermally driven cavity is a standard test-case for variable-density solvers [68]. Specially, in the context of natural convection [54, 76]. Benchmark solutions of [77] – using a fully compressible Navier-Stokes solver over a high-resolution mesh – will be used as reference.

Consider a differentially heated square cavity with side length \hat{L} , as presented in Fig. 6. Left and right walls are held at distinct temperatures, \hat{T}_H and \hat{T}_C , respectively, with $\hat{T}_H > \hat{T}_C$. Horizontal walls are perfectly insulated (adiabatic), i.e., with null thermal energy flux by them.

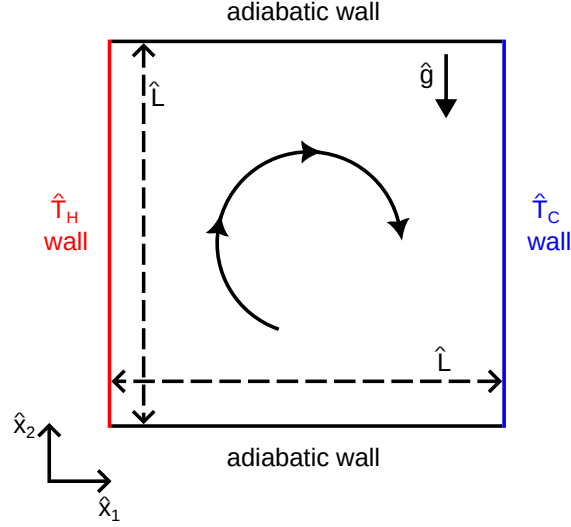


Figure 6: Scheme of enclosed square cavity of area \hat{L}^2 , under thermally induced flow. The left wall is maintained at temperature \hat{T}_H , and the right wall, at \hat{T}_C , with $\hat{T}_H > \hat{T}_C$. Horizontal walls are considered adiabatic.

For a buoyancy-driven flow, it is relevant to define the Rayleigh number (Ra). Namely,

$$\text{Ra} := \text{Pr} \frac{\hat{g}_c \hat{\rho}_c^2 (\hat{T}_H - \hat{T}_C) \hat{l}_c^3}{\hat{T}_c \hat{\mu}_c^2}, \quad (106)$$

which represents the relative importance between convection and thermal diffusion (or conduction). In fact, a $\text{Ra} \gg 1$ ($\text{Ra} \ll 1$) condition indicates a flow predominantly dictated by convection (conduction). Hence, it is the analogous of the Péclet number (Pe) for the free convection case, in which the flow is induced by density gradients.

The characteristic temperature is the mean temperature, i.e., $\hat{T}_c := (\hat{T}_H + \hat{T}_C)/2$, which permits the definition of the dimensionless temperature difference as

$$\epsilon := \frac{\hat{T}_H - \hat{T}_C}{2\hat{T}_c} \quad (107)$$

Note that it quantifies the influence of the temperature on the flow field not directly related to buoyancy effects [77]. Because of this, as ϵ increases, the Boussinesq approximation becomes invalid, while the present formulation can handle arbitrary temperature differences (respecting the limits of numerical stability). To demonstrate it, the greatest value of temperature difference (i.e., $\epsilon = 0.6$) will be considered here.

A characteristic velocity can be induced from the solution for natural convection along a vertical wall [78]: $\hat{v}_c := \text{Ra}^{1/2} \hat{\mu}_c / (\hat{\rho}_c \hat{l}_c)$, in which $\hat{\mu}_c := \hat{\mu}(\hat{T}_c)$, $\hat{\rho}_c := \hat{\rho}(\hat{T}_c)$ and $\hat{l}_c := \hat{L}$ [77]. A reference hydrodynamic pressure is also derived from this scales as $\hat{p}_c := \hat{\rho}_c \hat{v}_c^2$. Therefore, it is possible to relate the Rayleigh number (Ra) to the Péclet number (Pe) as [68]

$$\text{Pe} = \text{Pr} \text{Ra}^{1/2} \quad (108)$$

and, also, the Froude number (Fr) is obtained as [68]

$$\text{Fr} = (\text{Pr} 2\epsilon)^{1/2} \quad (109)$$

For a consistent comparison, $\text{Pr} = 0.71$, $\gamma = 1.4$, and the Sutherland's law [42] is considered to model transport coefficients, i.e.,

$$\kappa(T) = T^{3/2} \frac{1 + C}{T + C}, \quad (110)$$

in which $C := \hat{C}/\hat{T}_c$, with $\hat{C} = 110.5$ K denoting a substance-dependent constant, in this case, air.

An initial (characteristic) thermodynamic state is specified by $\hat{p}_{0,c} = 101\,325$ Pa, $\hat{T}_c = 600$ K and $\hat{\rho}_c = \hat{\rho}(\hat{p}_{0,c}, \hat{T}_c)$, which, in conjunction with the pair (Ra, ϵ) , is sufficient to describe the complete state of the system. In fact, hydrodynamic conditions are imposed from Ra, and dimensionless temperatures $T_H = (1 + \epsilon) = 1.6$ and $T_C = (1 - \epsilon) = 0.4$ are implicit in ϵ .

To recapitulate, for an enclosed domain, the thermodynamic pressure (p_0) evolves as (see Sec. 2)

$$p_0 = \frac{m}{\int_V T^{-1} dV} \quad (111)$$

in which m is the initial (dimensionless) mass, a constant.

Finally, in a problem of ‘‘heat transfer’’, it is convenient and representative to work in terms of the Nusselt number (Nu), which quantifies the enhancement of thermal energy transfer due to fluid motion relative to conduction alone. Its local version is defined by

$$\text{Nu}(x_2) := \frac{1}{2\epsilon} \left(\text{Pe} \rho v_1 T - \kappa \frac{\partial T}{\partial x_1} \right) \quad (112)$$

and, its spatially average (over a vertical profile), as

$$\overline{\text{Nu}} := \int_{x_2=0}^{x_2=1} \text{Nu} dx_2 \quad (113)$$

Boundary conditions. For the convenient choice of $Q = S + 1$,

$$v_1 = v_2 = Z = H - (T_H + 1) = 0 \quad , \quad \text{on the left wall } (x_1 = 0); \quad (114a)$$

$$v_1 = v_2 = Z = H - (T_C + 1) = 0 \quad , \quad \text{on the right wall } (x_1 = 1); \quad (114b)$$

$$v_1 = v_2 = Z = \frac{\partial H}{\partial x_2} = 0 \quad , \quad \text{on the horizontal walls } (x_2 = 0 \text{ and } x_2 = 1). \quad (114c)$$

Initial condition. A quiescent system, under the mean temperature ($T = 1$), composed by a uniform, non-reacting gaseous mixture (air),

$$v_1 = v_2 = Z = H - 2 = 0 \quad , \quad \text{at } t = 0 \quad (115)$$

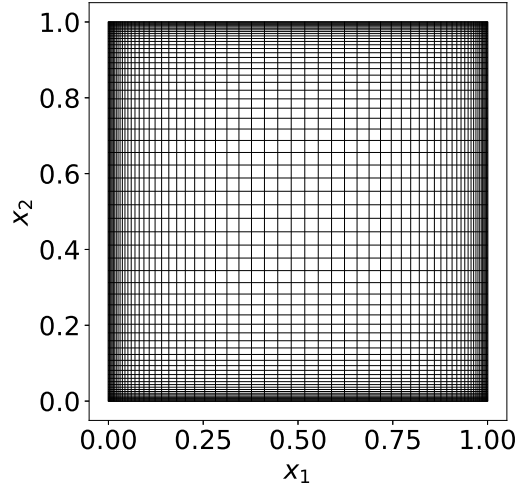


Figure 7: Non-uniformly spaced grid for a unity square, with increased resolution of twenty-one (21) times near boundary.

The verification is performed by comparing the results, for $(\text{Ra}, \varepsilon) = (10^n, 0.6)$ with $n \in \{2, 7\}$, against those from [77]. These two cases were chosen as they represent the two extremes, with the highest relative contributions from diffusion and convection, respectively. In this sense, intermediate cases, i.e., $n \in \{3, 4, 5, 6\}$, do not provide additional information and are, therefore, omitted. Note that for both cases, the flow is in the steady state, considered here when temporal derivative of the thermodynamic pressure (p_0) is, at least, as small as 10^{-6} . In fact, due to its “global nature”, p_0 is an appropriate choice for monitoring global convergence, including for the steady state, grid resolution, and other related factors.

4.4.1. Grid convergence study

Table 3: Grid convergence study for $\text{Ra} = 10^2$.

Grid	$\max(\Delta_{x_i})$	p_0	GCI	GCI ratio
64×64	0.019 59	0.957 52	–	–
96×96	0.013 03	0.957 44	0.009%	–
144×144	0.008 68	0.957 40	0.004%	2.236
216×216	0.005 78	0.957 38	0.002%	2.241

The order of convergence (a) is estimate as $a = 1.99$, using values of the most refined grids in Eq. (98), with refinement ratio $\delta = 1.5$;

GCI is the grid convergence index, as defined in Eq. (99).

Calculated on non-uniform grid such as $\min(\Delta_{x_i}) = \max(\Delta_{x_i})/2$ for $i = 1, 2$.

Table 4: Grid convergence study for $Ra = 10^7$.

Grid	$\max(\Delta_{x_i})$	p_0	GCI	GCI ratio
64×64	0.035 73	0.919 90	–	–
96×96	0.023 72	0.921 38	0.170	–
144×144	0.015 77	0.922 08	0.080	2.126
216×216	0.010 49	0.922 40	0.037	2.180

The order of convergence (a) is estimated as $a = 1.92$, using values of the most refined grids in Eq. (98), with refinement ratio $\delta = 1.5$;

GCI is the grid convergence index, as defined in Eq. (99).

Calculated on non-uniform grid such as $\min(\Delta_{x_i}) = \max(\Delta_{x_i})/21$ for $i = 1, 2$.

Simulations are performed over non-uniform grids, with accumulation of points near walls, for numerical efficiency. Indeed, the resolution at the boundary region can be refined using the hyperbolic tangent transformation, given by

$$\tilde{x}_i = \frac{1 + \tanh[\alpha(x_i - 1/2)]}{2 \tanh(\alpha/2)}, \quad (116)$$

for each direction (i.e., $i = 1, 2$). The real constant α controls the grid clustering intensity. As $\alpha \rightarrow 0$, the transformation tends to the identity transformation. As α increases, the accumulation becomes more pronounced near the domain boundary. The parameter α is determined numerically to achieve a specified spacing ratio (e.g., 10 for tenfold resolution enhancement at boundaries).

This analysis, as justified above, is based on the hydrodynamic pressure (p_0). Tables 3 and 4 synthesise the finds of the grid convergence study, for the cases $Ra = 10^2$ and 10^7 , respectively. The grid partition is the same for both directions ($i = 1, 2$), with $\max(\Delta_{x_i}) = m \min(\Delta_{x_i})$ in the interior region, with $m = 2$ for $Ra = 10^2$, and $m = 21$ for $Ra = 10^7$. Both cases encompass fourth grid resolutions, departing from 64×64 to 216×216 , with a refinement ratio of $\delta = 1.5$. The accumulation of points in the proximity of boundary is much more pronounced for the case $Ra = 10^7$ (21 times the interior resolution), because it requires more resolution to describe, properly, variations inside the thin thermal boundary layer, i.e., to capture strong gradients near walls. As evidenced, the order of convergence is compatible with a second-order method. Furthermore, it is possible to infer the importance of a non-uniform grid, refined only in the required regions, for efficient computation. With relatively fewer degrees of freedom, results are very close to those of the reference, as will be presented in the next section.

4.4.2. Results comparison

This verification is organised into three levels. The first level involves visualising streamlines and isotherms, which provides a more qualitative check. It is presented in Fig. 8, for both cases ($Ra = 10^2$ and 10^7). The second level addresses the local profiles of relevant properties. Since these data are only available in graphical form, they have been extracted using an appropriate tool [79]. This process inevitably introduces uncertainty, depending on factors such as figure resolution and line width, but it enables a systematic comparison of variables behaviour. Figures 9

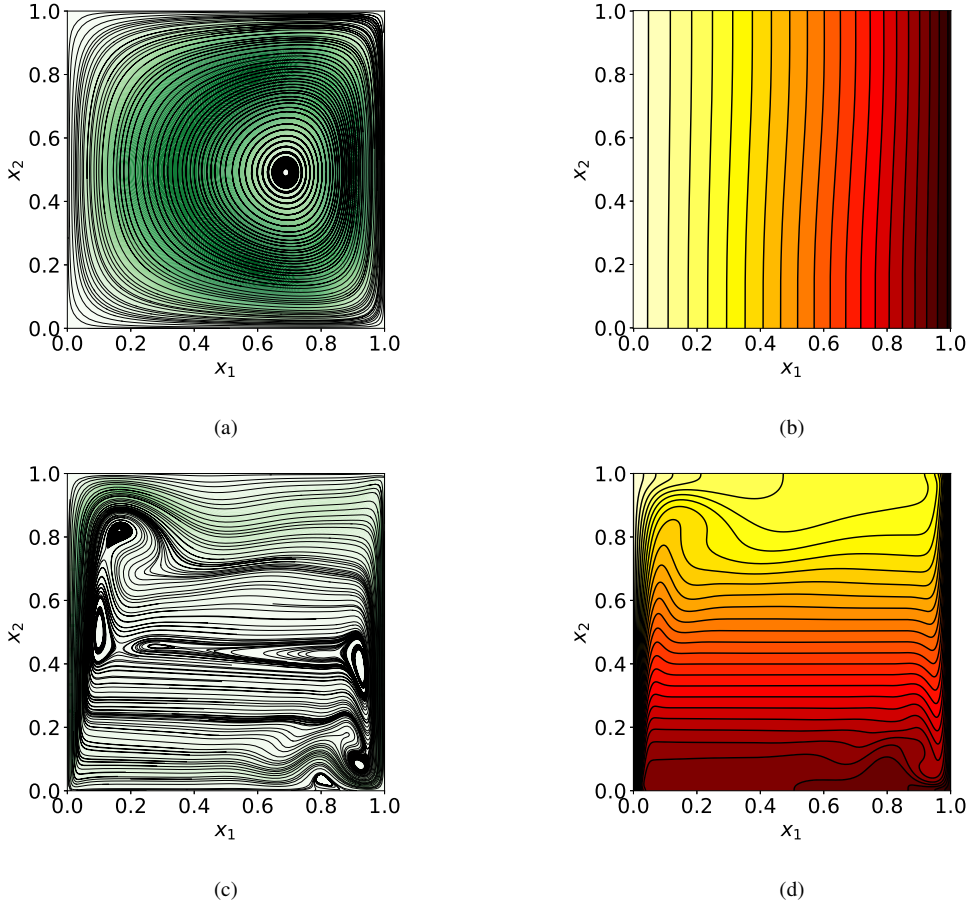


Figure 8: Streamlines – (a) and (c) – and isotherms – (b) and (d) – for a qualitative verification of cases $Ra = 10^2$ and $Ra = 10^7$, respectively. Light (dark) regions indicate areas of low (high) speed or high (low) temperatures.

and 10 show the computed profiles (represented by lines) in comparison with the reference profiles (represented by marks), for the smaller and greater Rayleigh number, respectively. It should also be noted that, at low Mach number limit, the flow responds only to pressure differences, meaning that any solution with the correct pressure gradient is sufficient. However, to enable a direct comparison with the reference, (hydrodynamic) pressures must be aligned to the same baseline. Therefore, data obtained with the present formulation was shifted to match the reference pressure baseline, using the average between the maximum and minimum profile values as a basis for this adjustment. The third level provides a more rigorous quantitative verification by comparing the values of key (global) parameters to those tabulated in the reference, as compiled in Tab. 5.

In short, the calculated and reference solutions show consistent agreement across all levels of analysis, verifying the proper modelling of energy transfer processes, and the code correctness.

4.5. Double Tsuji flame

This case is a complete test for the proposed method. Consider an infinitely long circular cylindrical burner, with radius \hat{R} , that radially and uniformly ejects fuel, with mass fraction $\hat{Y}_{F,b}$

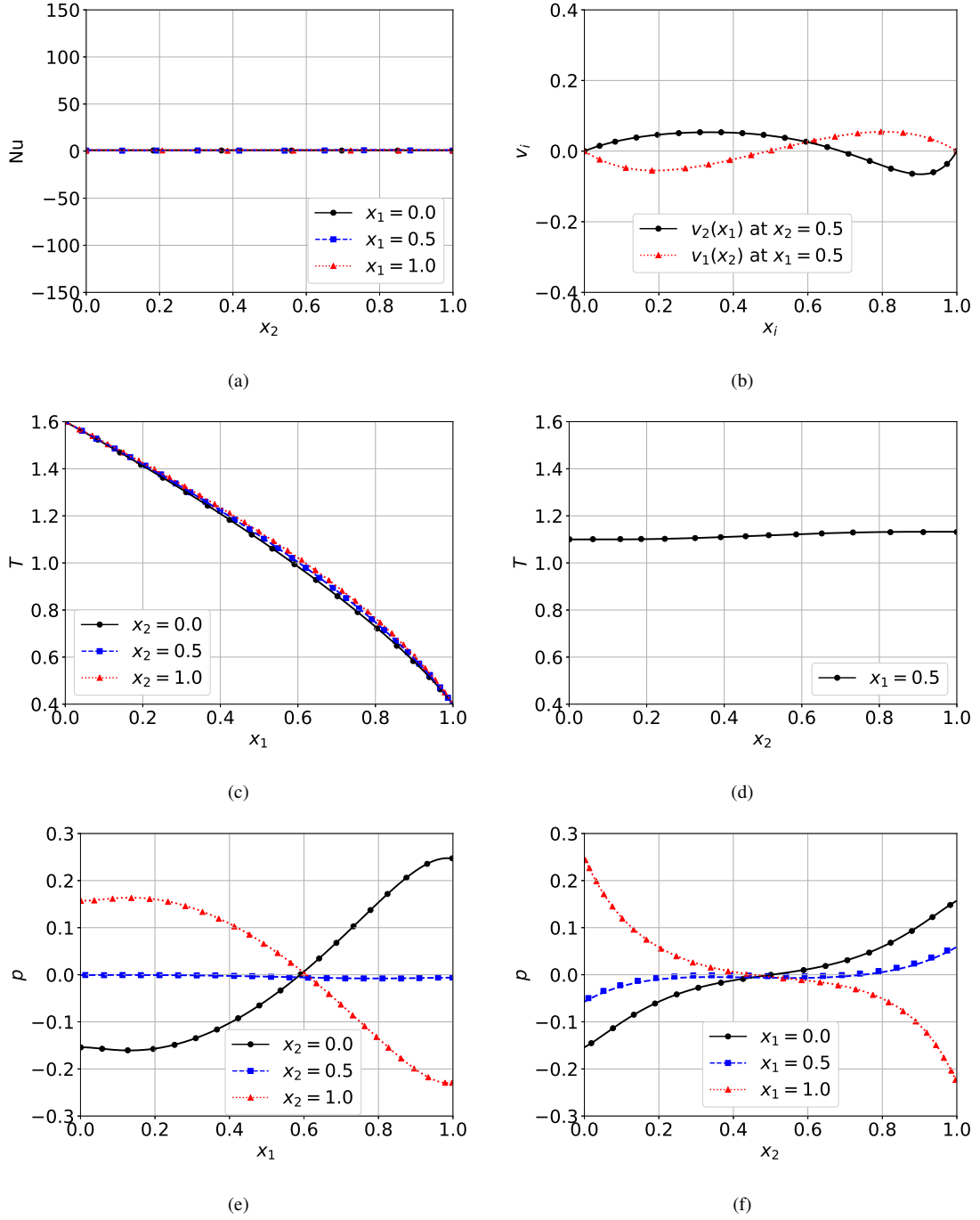


Figure 9: Profiles of local Nusselt number, Nu (a) ; vertical, v_2 , and horizontal, v_1 , velocity components (b), temperature, T , over horizontal (c) and vertical (d) axes; and hydrodynamic pressure, p , over horizontal (e) and vertical (f) axes. Lines indicate computed profiles over a 216×216 grid, while markers denote reference profiles, for $Ra = 10^2$.

and velocity magnitude \hat{u}_b , in the centre of an atmosphere generated by planar impinging jets, composing a counterflow of oxidiser, with a mass fraction $\hat{Y}_{O,\infty}$ and strain rate \hat{a} . This setup is

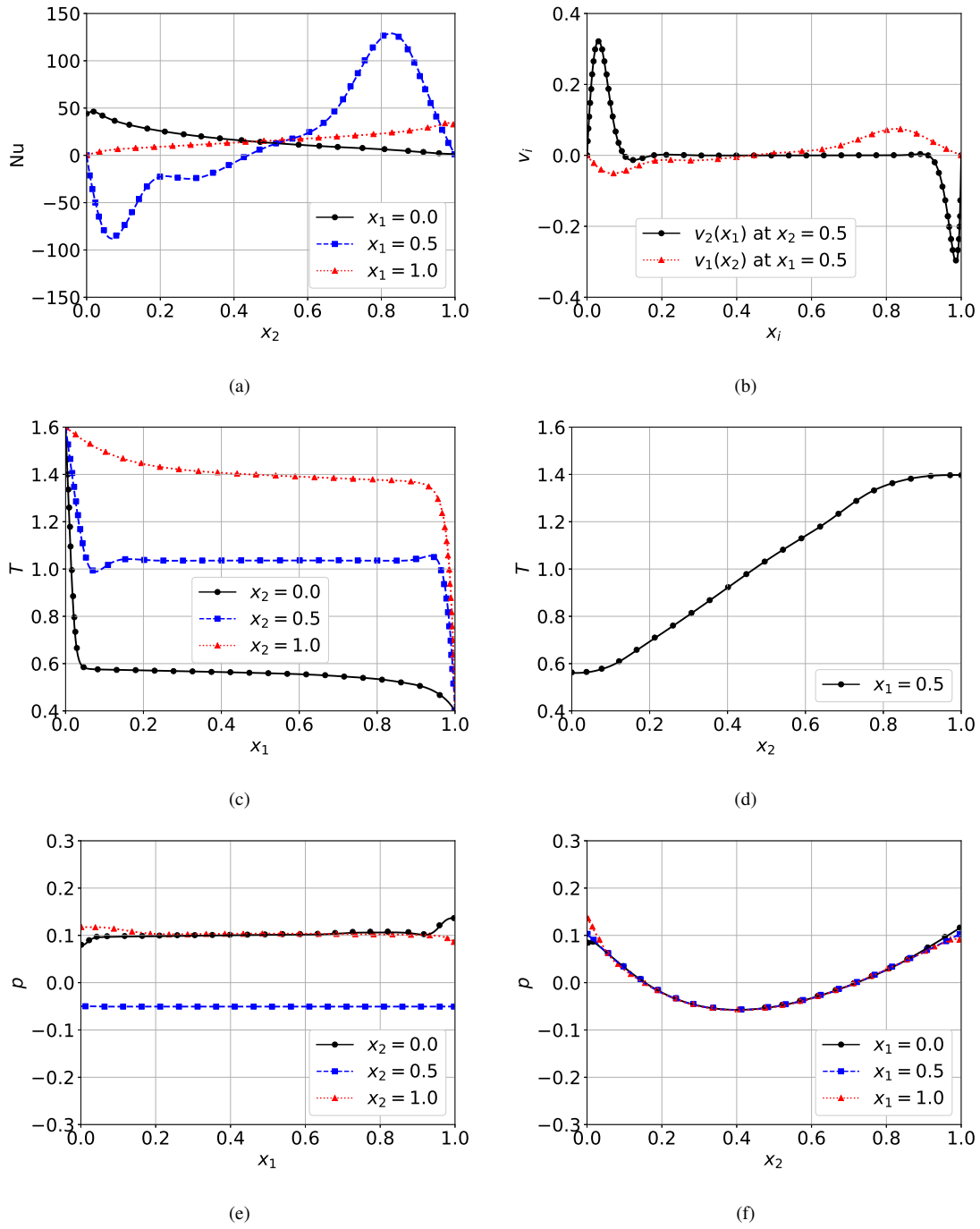


Figure 10: Profiles of local Nusselt number, Nu (a), ; vertical, v_2 , and horizontal, v_1 , velocity components (b), temperature, T , over horizontal (c) and vertical (d) axes; and hydrodynamic pressure, p , over horizontal (e) and vertical (f) axes. Lines indicate computed profiles over a 216×216 grid, while markers denote reference profiles, for $Ra = 10^7$.

referred to as the double Tsuji burner, and the resulting flame is known as the double Tsuji flame

Table 5: Comparison of global properties.

Ra	Data Type	p_0	$\overline{\text{Nu}}_L$	$\overline{\text{Nu}}_M$	$\overline{\text{Nu}}_R$
10^2	Calculated	0.95738	0.9787	0.9787	0.9786
	Reference	0.95736	0.9787	0.9787	0.9787
10^7	Calculated	0.92245	16.248	16.241	16.222
	Reference	0.92263	16.241	16.241	16.240

Simulations performed on non-uniformly spaced grid (216×216), with distinct accumulation of points (near walls) for each case: 2 : 1 for $\text{Ra} = 10^2$, and 21 : 1 for $\text{Ra} = 10^7$.

$\overline{\text{Nu}}_A$ denotes spatially averaged Nusselt number at left ($A = L$), middle ($A = M$), and right ($A = R$) walls.

Reference data from [77].

[80, 81].

Double Tsuji flames exhibit characteristics of both counterflow and coflow diffusion flames, with smooth transitions between these behaviours across their spatial distribution [80, 82]. As such, they can be regarded as a “generalised flame”, encapsulating features of flames under diverse flow conditions, within a single configuration. This makes them an ideal test case for verifying numerical methods for reacting flow simulations. Additionally, the cylindrical burner with radial ejection introduces a geometric complexity that demands a proper technique to represent such configuration on orthogonal meshes. In fact, to accomplish it, an immersed boundary method (IBM) with mass flux, as described in Sec. 3.4, is employed.

To consider the radial fuel ejection from the burner, a linear source of mass (S_m) is added to the continuity equation, consistently with the fuel ejection velocity. More specifically,

$$S_m(x_1, x_2) := \chi \frac{\rho_b U_b}{(x_1^2 + x_2^2)^{1/2}}, \quad (117)$$

together with a radial ejection velocity

$$v_{ib_j}(x_1, x_2) := \frac{U_b}{(x_1^2 + x_2^2)^{1/2}} x_j \quad (118)$$

for $j = 1, 2$. Mixture fraction (Z_{ib}) and excess enthalpy (H_{ib}), at the burner, are given by

$$Z_{ib} = S + 1 \quad , \quad H_{ib} = (S + 1)/Q + 1 \quad (119)$$

For next discussions, in the absence of an explicit definition, the following parameters are considered: $\text{Pr} = 0.71$, $\text{Pe} = 71$ (or $\text{Re} = 100$), $U_b = 0.1$, $S = 14.89$, $Q = 4.17$, $\text{Le}_F = 0.97$, $\text{Le}_O = 1.11$, with $\text{Da}_{ib} = 10^{-4}$ and $\varepsilon = 0.5$.

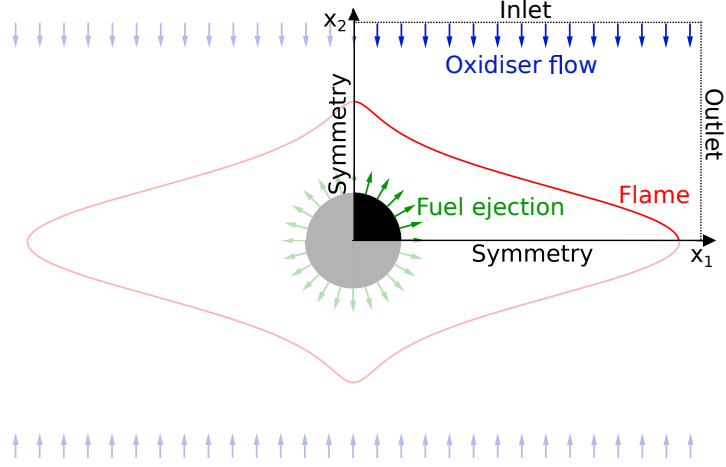


Figure 11: Schematic representation of the double Tsuji burner: an infinitely long cylinder (2D represented), which ejects fuel radially and evenly, placed in the centre of impinging oxidant flows (a planar unconfined counterflow). By symmetry, the first quadrant represents totally the system, a priori.

Boundary conditions.

$$v_1 = \partial_{x_1} v_2 = \partial_{x_1} Z = \partial_{x_1} H = 0 \quad , \quad \text{on the vertical symmetry axis } (x_1 = 0); \quad (120a)$$

$$\partial_{x_2} v_1 = v_2 = \partial_{x_2} Z = \partial_{x_2} H = 0 \quad , \quad \text{on the horizontal symmetry axis } (x_2 = 0); \quad (120b)$$

$$v_1 - x_1 = v_2 + x_2 = Z - Z_\infty = H - H_\infty = 0 \quad , \quad \text{at the inlet } (x_2 \rightarrow \infty) \quad (120c)$$

$$\partial_{x_1} v_1 = \partial_{x_1} v_2 = \partial_{x_1} Z = \partial_{x_1} H = 0 \quad , \quad \text{at the outlet } (x_1 \rightarrow \infty). \quad (120d)$$

in which $Z_\infty := 0$ and $H_\infty := (S + 1)/Q + 1$.

For an open domain, such as in the present case, global mass conservation (throughout the computational domain) can be challenging. Since the scope of this study is not directly related to boundary conditions, a simple outflow extrapolation is imposed, as defined above. Global mass conservation is, then, monitored, with the outlet flux being uniformly modified, as necessary.

Initial condition. Temporal integration initiates from a potential flow [80, 82]:

$$v_1(x_1, x_2) = x_1 \left[1 - \frac{(x_1^2 - 3x_2^2)}{(x_1^2 + x_2^2)^3} + \frac{U_b}{x_1^2 + x_2^2} \right]; \quad (121a)$$

$$v_2(x_1, x_2) = -x_2 \left[1 + \frac{(3x_1^2 - x_2^2)}{(x_1^2 + x_2^2)^3} - \frac{U_b}{x_1^2 + x_2^2} \right], \quad (121b)$$

and asymptotic solutions for Z and H [80], modified to also include the ejection effect:

$$Z(x_1, x_2) = \left[\frac{1 + U_b/w_F^2}{(x_1/w_F)^2 + U_b/w_F^2} \right]^{1/2} \exp(-x_2^2/2) \quad (122a)$$

$$H(x_1, x_2) = \left[\frac{S + 1}{Q} (T_F - 1) - 1 \right] Z + \frac{S + 1}{Q} + 1 \quad (122b)$$

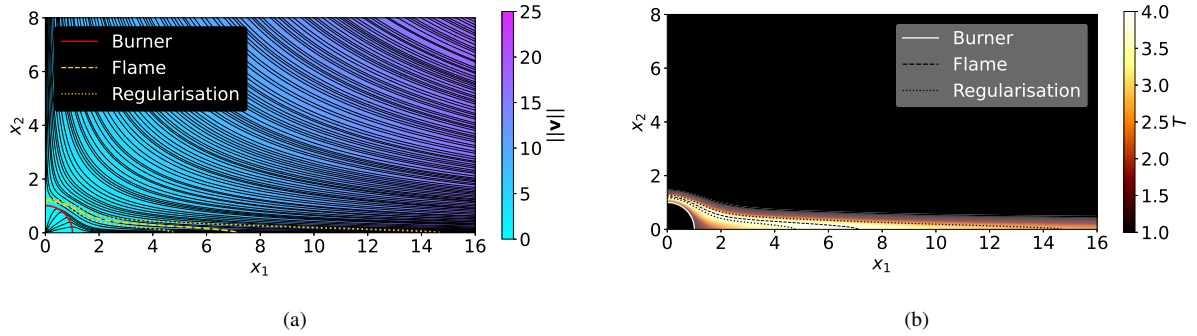


Figure 12: Streamlines with velocity magnitude indication (a) and temperature field for the double Tsuji burner. Light (dark) portions indicate low (high) speed or high (low) temperatures.

in which w_F and T_F are the width (location on the x_1 -axis) and temperature of the flame, estimated in the reference.

4.5.1. Steady-state solution

Flow topology, velocity and temperature are presented in Fig. 12. As the effect of impinging flows, strong variations of velocity and temperature are confined to the stagnation region (over x_2 -axis), and around the x_1 -axis. Additional lines illustrate the cylinder surface (solid line), flame position (dashed line), and flame regularisation thickness (between dotted lines).

4.5.2. Domain size dependence

Table 6: Domain convergence study.

Parameter	Value	h_F	$\Delta h_F(\%)$	w_F	$\Delta w_F(\%)$
L_{x_1}	10	1.219 69	–	7.132 64	–
	15	1.219 04	–0.053	7.108 68	–0.337
	20	1.219 00	–0.004	7.107 06	–0.023
<i>Horizontal Convergence ($L_{x_2} = 10$)</i>					
L_{x_2}	10	1.219 00	–	7.107 06	–
	15	1.220 72	0.141	7.120 96	0.195
	20	1.221 56	0.069	7.128 79	0.110
<i>Vertical Convergence ($L_{x_1} = 20$)</i>					

Δ : Relative change from previous domain size.

Consider L_{x_1} and L_{x_2} as the numerical domain size in the (horizontal) x_1 -direction and the (vertical) x_2 -direction, respectively. A non-uniform grid is generated for the domain $[0, L_{x_1}] \times [0, L_{x_2}]$, with $L_{x_i} = 20$ ($i = 1, 2$) and resolution 700×700 . The most refined regions are around symmetry axes, with grid spacing as small as $\Delta x_i = 5 \times 10^{-3}$ for both directions (i.e., $i = 1, 2$). That is, the burner regions is the most refined one. The coarsest region is in the outlet vicinity, for

the horizontal spacing (Δx_1), and around the inlet, for the vertical spacing (Δx_2), with $\Delta x_i \approx 0.1$ for $i = 1, 2$. Taking subsets of this initial grid, the following subdomains length are considered for the domain size dependence test: $L_{x_1} = 10, 15$ and 20 with $L_{x_2} = 10$, for the horizontal direction; $L_{x_2} = 10, 15$ and 20 with $L_{x_1} = 20$, for the vertical direction. The flame positions on the horizontal (w_F) and vertical (h_F) axes are selected as the monitoring parameters, denoted as the flame width and height, in this order. As shown in Tab. 6, increasing the horizontal domain, from $L_{x_1} = 15$ to 20 , resulted in a maximum relative variation of $\Delta w_F \approx -0.02\%$ in the flame width, and $\Delta h_F \approx -0.004\%$ in its height. For an equivalent decrease in the vertical domain, from $L_{x_2} = 15$ to 10 , a maximum relative variation of $\Delta w_F = -0.19\%$ in the flame width, and $\Delta h_F = -0.14\%$ in its height, are also observed in Tab. 6. Given the observed small deviations, and the convergence trend, a domain size of $L_{x_1} = 20$ and $L_{x_2} = 10$ ensures that boundary effects arising from domain truncation alter relevant parameters by no more than 0.2% . This meets a rigid domain size convergence criterion, and consequently, this domain will be employed in all subsequent simulations.

4.5.3. Parameters dependence

Table 7: Parameters convergence study.

Parameter	Value	h_F	$\Delta h_F(\%)$	w_F	$\Delta w_F(\%)$
Da_{ib}	$1.6 \cdot 10^{-4}$	1.212 61	–	7.215 02	–
	$8 \cdot 10^{-5}$	1.221 25	0.707	7.071 52	–2.029
	$4 \cdot 10^{-5}$	1.225 75	0.367	6.998 39	–1.045
ε	0.9	1.218 78	–	7.125 82	–
	0.5	1.219 01	–0.019	7.106 95	0.265
	0.1	1.219 13	–0.010	7.088 65	0.258

Δ : Relative change from previous parameter value.

The effects of the IB Darcy number (Da_{ib}) and the flame regularisation thickness (ε) are accessed here.

IB Darcy number. As inferred from the discussion for the Taylor–Couette flow (refer to Sec. 4.3), $Da_{ib} = 10^{-4}$ is a good starting point. In addition, the values $Da_{ib} = 1.6 \cdot 10^{-4}, 8 \cdot 10^{-5}$ and $4 \cdot 10^{-5}$ are tested. The first part of Tab. 7 compiles the results. Solutions are little sensitive to the variations of Da_{ib} in that interval, with maximum variations of 2% .

Flame regularisation. The regularisation of the flame is conveniently done around the stoichiometric level of the mixture fraction (i.e. $Z = 1$), rather than directly around the spatial position of the flame (refer to Sec. 3.5). This approach simplifies mathematical modelling and numerical implementation, but does not allow precise spatial control of the regularisation thickness, a priori, as illustrated by the region delimited by dotted lines in Fig. 12. Nonetheless, this approach proved to be efficient and sufficiently accurate, with little sensitivity to the regularisation thickness (ε), according to the results for $\varepsilon = 0.1, 0.5$ and 0.9 , in the second part of Tab. 7.

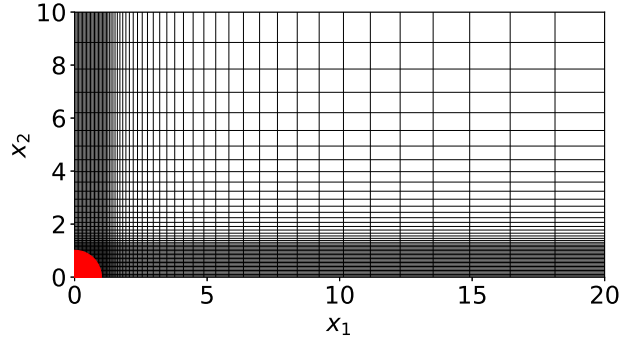


Figure 13: Illustration of the grid topology used for double-Tsuji-burner simulations. The circular cylindrical burner is represented by a filled circle at the origin.

4.5.4. Grid resolution dependence

Table 8: Grid convergence study.

Resolution	h_F	$\Delta h_F(\%)$	w_F	$\Delta w_F(\%)$
600×480	1.219 01	–	7.106 95	–
900×720	1.218 97	–0.003	7.106 83	–0.002

Δ : Relative change from previous grid resolution.

In this case, strongest gradients are concentrated in the stagnation region, upstream the cylinder, and around the flame sheet. Thus, a grid with variable refinement is used, with augmented resolution in those zones, as depicted in Fig. 13. Results are synthesised in Tab. 8. The relative variations from 600×480 to 900×720 are very small, attesting that the results are, asymptotically, converged.

4.5.5. OpenFOAM comparison

Results obtained from the present approach are compared with that from OpenFOAM 8. The same hypotheses admitted in Sec. 2 are imposed in OpenFOAM simulations. Since this functionality was unavailable in standard libraries, the power law for the transport coefficients was implemented. Additionally, constant Lewis numbers (Le_i) for each species (i) of a complete methane reaction were specified using the reactingLeFoam solver [83], with values specified in [41].

As exhibited in Fig. 14, a very good agreement of flame shapes and isotherms are obtained. Minor deviations were expected and can be attributed to the inherent distinctions in the numerical methods employed by the respective solver (e.g., spatial and operator discretisations, flame regularisation procedures, and the circular cylinder representations). Therefore, the properness and accuracy of the proposed methods are established.

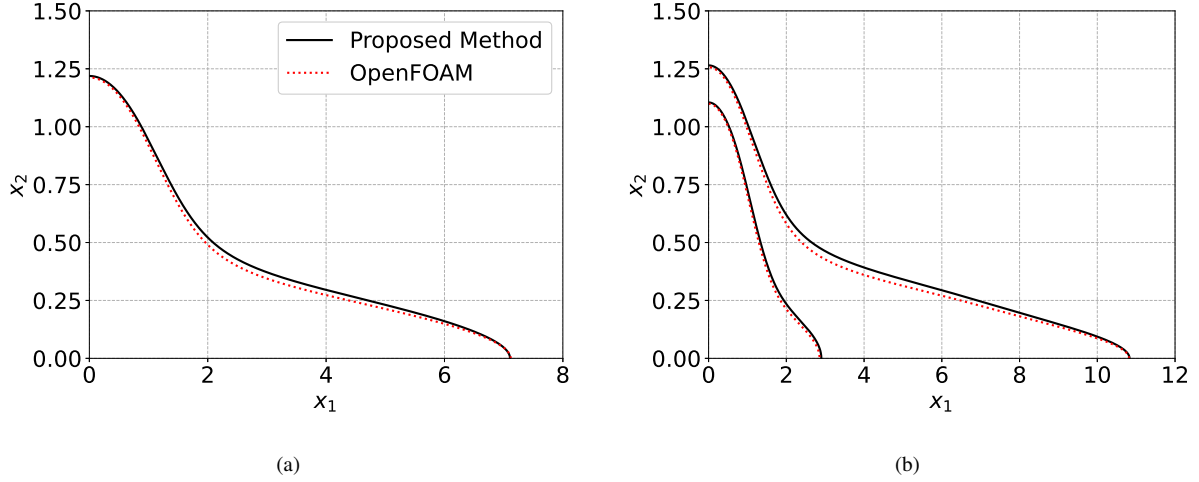


Figure 14: Comparison between flame shape (a) and the isotherm $T = 3$ (b) from simulations using the proposed method and OpenFOAM.

5. Conclusion

This work proposes a robust numerical method for simulations of low-Mach-number flows, ranging from incompressible to strongly-variable density ones, without and with combustion. The numerical approach is based on the transformation of the original set of partial differential equations, using spatial discretisation, into a set of ordinary differential equations (method of lines). Thus, a predictor-corrector scheme could be applied to them, using a fractional time-step (or projection) method to couple pressure and velocity. It consists in the solution of a Poisson equation for pressure, whose boundary conditions are inherited from the interfaces fluxes, when based on staggered or collocated grids with the definition of auxiliary fluxes. A second-order Adams–Bashforth (Adams–Moulton) temporal scheme is used for the predictor (corrector) stage. Equations are spatially discretised into a collocated grid using centred finite differences, specially designed to produce strong “odd-even coupling”, via interpolation of auxiliary fluxes. A regularisation technique for flame properties is proposed to mitigate the discontinuity issue, induced by the flame sheet approximation. A new feature of it is the regularisation based on the temperature derivative, from which the singularity effectively emerges, rather than directly on temperature, as classically performed. Another relevant contribution is the extension of the immersed boundary method (IBM) to consider mass fluxes from the immersed body surfaces, which naturally demands a mass source addition to the continuity equation. Selected test cases demonstrated the capability and limitations of the method under different conditions, focusing on distinct aspects. Namely, the correctness and accuracy of the projection method are tested using Taylor–Green vortices. IBM is analysed using a Taylor–Couette flow, providing insightful conclusions about the penalisation method and related parameters selection. The capability to handle strong density gradients and thermal-energy transport is verified in a differentially heated cavity. Finally, the composition of these various methods, including IBM for velocity, mixture fraction and excess enthalpy, species mass transport, differential-preferential diffusion, and flame regularisation are checked using the

double Tsuji flame. After the complete discussion of this work, it is possible to state that the proposed numerical method is stable, efficient and accurate.

Declaration of Competing Interest

No potential conflict of interest was reported by the authors.

Acknowledgments

This article is dedicated to the memory of Professor Amable Liñán.

This study was financed, in part, by the São Paulo Research Foundation (FAPESP), Brasil. Process Numbers 2021/09246-9, 2021/10689-2 and 2022/14361-4. This study was financed, in part, the Conselho Nacional de Desenvolvimento Científico e Tecnológico (CNPq) – under grants 307922/2019-7, 161887/2021-0, and 301607/2025-7; This study was financed, in part, by the Coordenação de Aperfeiçoamento de Pessoal de Nível Superior – Brasil (CAPES) – Finance Code 001. D.R. acknowledges funding by MCIN/AEI/10.13039/501100011033 and the European Union’s FEDER (Funder ID: 10.13039/501100011033), under grant PID2024-157642MB-I00. Research carried out using the computational resources of the Center for Mathematical Sciences Applied to Industry (CeMEAI) funded by FAPESP (grant 2013/ 07375-0).

References

- [1] B. Müller, Low-Mach-number asymptotics of the Navier–Stokes equations, in: *Floating, Flowing, Flying*, Springer, 1998, pp. 97–109.
- [2] S. Glegg, W. Devenport, *Aeroacoustics of low Mach number flows: fundamentals, analysis, and measurement*, Academic Press, 2017.
- [3] R. Klein, Semi-implicit extension of a Godunov-type scheme based on low Mach number asymptotics I: One-dimensional flow, *Journal of Computational Physics* 121 (2) (1995) 213–237.
- [4] N. Happenhofer, H. Grimm-Strele, F. Kupka, B. Löw-Baselli, H. Muthsam, A low Mach number solver: Enhancing applicability, *Journal of Computational Physics* 236 (2013) 96–118.
- [5] A. Majda, *Compressible fluid flow and systems of conservation laws in several space variables*, Vol. 53, Springer, 1984.
- [6] T. Alazard, Low Mach number limit of the full Navier–Stokes equations, *Archive for Rational Mechanics and Analysis* 180 (2006) 1–73.
- [7] T. Alazard, Low Mach number flows and combustion, *SIAM Journal on Mathematical Analysis* 38 (4) (2006) 1186–1213.
- [8] J. R. Clausen, Entropically damped form of artificial compressibility for explicit simulation of incompressible flow, *Physical Review E* 87 (2013) 013309. doi:10.1103/PhysRevE.87.013309.
- [9] T. Alazard, A minicourse on the low Mach number limit, *Discrete and Continuous Dynamical Systems-Series S* 1 (3) (2008) 365–404.

- [10] B. Lessani, M. V. Papalexandris, Time-accurate calculation of variable density flows with strong temperature gradients and combustion, *Journal of Computational Physics* 212 (1) (2006) 218–246.
- [11] C. Wall, C. D. Pierce, P. Moin, A semi-implicit method for resolution of acoustic waves in low Mach number flows, *Journal of Computational Physics* 181 (2) (2002) 545–563.
- [12] I. Keshtiban, F. Belblidia, M. Webster, Compressible flow solvers for low Mach number flows – a review, *International Journal for Numerical Methods in Fluids* 23 (2004) 77–103.
- [13] E. Turkel, Preconditioning techniques in computational fluid dynamics, *Annual Review of Fluid Mechanics* 31 (1999) 385–416.
- [14] A. J. Chorin, A numerical method for solving incompressible viscous flow problems, *Journal of Computational Physics* 2 (1) (1967) 12–26.
- [15] A. J. Chorin, Numerical solution of the Navier–Stokes equations, *Mathematics of Computation* 22 (104) (1968) 745–762.
- [16] R. Temam, Sur l’approximation de la solution des équations de Navier–Stokes par la méthode des pas fractionnaires (i), *Archive for Rational Mechanics and Analysis* 32 (1969) 135–153.
- [17] D. Dupuy, A. Toutant, F. Bataille, Artificial compressibility method for strongly anisothermal low Mach number flows, *Physical Review E* 103 (2021) 013314. doi:10.1103/PhysRevE.103.013314.
- [18] P. Madsen, H. Schäffer, A discussion of artificial compressibility, *Coastal Engineering* 53 (1) (2006) 93–98.
- [19] S. MacNamara, G. Strang, Operator splitting, in: R. Glowinski, S. J. Osher, W. Yin (Eds.), *Splitting Methods in Communication, Imaging, Science, and Engineering*, Springer International Publishing, Cham, 2016, pp. 95–114.
- [20] J. Perot, An analysis of the fractional step method, *Journal of Computational Physics* 108 (1) (1993) 51–58.
- [21] J. Perot, Comments on the fractional step method, *Journal of Computational Physics* 121 (1) (1995) 190–191.
- [22] C. S. Peskin, Flow patterns around heart valves: a numerical method, *Journal of Computational Physics* 10 (2) (1972) 252–271.
- [23] C. S. Peskin, The immersed boundary method, *Acta Numerica* 11 (2002) 479–517. doi:10.1017/S0962492902000077.
- [24] R. Verzicco, Immersed boundary methods: Historical perspective and future outlook, *Annual Review of Fluid Mechanics* 55 (2023) 129–155. doi:https://doi.org/10.1146/annurev-fluid-120720-022129.
- [25] R. Mittal, G. Iaccarino, Immersed boundary methods, *Annual Review of Fluid Mechanics* 37 (2005) 239–261. doi:https://doi.org/10.1146/annurev.fluid.37.061903.175743.
- [26] W. Iwakami, Y. Yatagai, N. Hatakeyama, Y. Hattori, A new approach for error reduction in the volume penalization method, *Communications in Computational Physics* 16 (5) (2014) 1181–1200. doi:10.4208/cicp.220513.070514a.
- [27] M. Specklin, Y. Delauré, A sharp immersed boundary method based on penalization and its application to moving boundaries and turbulent rotating flows, *European Journal of Mechanics – B/Fluids* 70 (2018) 130–147. doi:https://doi.org/10.1016/j.euromechflu.2018.03.003.
- [28] E. Arquis, J.-P. Caltagirone, Sur les conditions hydrodynamiques au voisinage d’une inter-

- face milieu fluide-milieu poreux: application a la convection naturelle, *CR Acad. Sci. Paris II* 299 (1) (1984).
- [29] D. Goldstein, R. Handler, L. Sirovich, Modeling a no-slip flow boundary with an external force field, *Journal of Computational Physics* 105 (2) (1993) 354–366. doi:<https://doi.org/10.1006/jcph.1993.1081>.
- [30] G. Iaccarino, R. Verzicco, Immersed boundary technique for turbulent flow simulations, *Applied Mechanics Reviews* 56 (3) (2003) 331–347. doi:10.1115/1.1563627.
- [31] S. P. Burke, T. E. W. Schumann, Diffusion flames, *Symposium (International) on Combustion* (1948) 2–11.
- [32] Y. B. Zeldovich, G. I. Barenblatt, V. B. Librovich, G. M. Makhviladze, *The Mathematical theory of combustion and explosions*, Consultants Bureau, New York, 1985.
- [33] A. Liñán, The structure of diffusion flames, in: M. Onofri, A. Tesi (Eds.), *Fluid Dynamic Aspects of Combustion Theory*, Longman Scientific & Technical, Harlow, Essex, 1991, pp. 11–29.
- [34] F. F. Fachini, An analytical solution for the quasi-steady droplet combustion, *Combustion and Flame* 116 (1) (1999) 302–306.
- [35] F. F. Fachini, A. Liñán, F. A. Williams, Theory of flame histories in droplet combustion at small stoichiometric fuel-air ratios, *AIAA J.* 37 (11) (1999) 1426–1435.
- [36] F. F. Fachini, Extended Shvab-Zel'dovich formulation for multicomponent-fuel diffusion flames, *Int. J. Heat Mass Transf.* 50 (2007) 1035–1048.
- [37] P. Angot, C.-H. Bruneau, P. Fabrie, A penalization method to take into account obstacles in incompressible viscous flows, *Numerische Mathematik* 81 (4) (1999) 497–520.
- [38] G. Carbou, P. Fabrie, Boundary layer for a penalization method for viscous incompressible flow, *Advances in Differential Equations* 8 (12) (2003) 1453 – 1480. doi:10.57262/ade/1355867981.
- [39] M. Kooshkbaghi, B. Lessani, A collocated grid, projection method for time-accurate calculation of low-Mach number variable density flows in general curvilinear coordinates, *International Journal for Numerical Methods in Fluids* 72 (3) (2013) 301–319. doi:<https://doi.org/10.1002/flid.3734>.
- [40] T. Poinot, D. Veynante, *Theoretical and numerical combustion*, AFNIL, 2022.
- [41] M. D. Smoke, V. Giovangigli, Formulation of the premixed and nonpremixed test problems, in: M. D. Smooke (Ed.), *Reduced Kinetic Mechanisms and Asymptotic Approximations for Methane-Air Flames: A Topical Volume*, Springer Berlin Heidelberg, Berlin, Heidelberg, 1991, pp. 1–28. doi:10.1007/BFb0035363.
- [42] W. Sutherland, On the viscosity of gases and molecular force, *The London, Edinburgh, and Dublin Philosophical Magazine and Journal of Science* 36 (223) (1893) 507–531. doi:10.1080/14786449308620508.
- [43] S. Schochet, The mathematical theory of low Mach number flows, *ESAIM: Mathematical Modelling and Numerical Analysis* 39 (3) (2005) 441–458.
- [44] A. Majda, J. Sethian, The derivation and numerical solution of the equations for zero Mach number combustion, *Combustion Science and Technology* 42 (3-4) (1985) 185–205.
- [45] G. I. Sivashinsky, Hydrodynamic theory of flame propagation in an enclosed volume, *Acta Astronaut.* 6 (5-6) (1979) 631–645.

- [46] M. V. Papalexandris, On the applicability of Stokes' hypothesis to low-Mach-number flows, *Continuum Mechanics and Thermodynamics* 32 (4) (2020) 1245–1249.
- [47] F. Nicoud, Conservative high-order finite-difference schemes for low-Mach number flows, *Journal of Computational Physics* 158 (1) (2000) 71–97.
- [48] F. Maria Denaro, On the application of the Helmholtz–Hodge decomposition in projection methods for incompressible flows with general boundary conditions, *International Journal for Numerical Methods in Fluids* 43 (1) (2003) 43–69.
- [49] H. N. Najm, P. S. Wyckoff, O. M. Knio, A semi-implicit numerical scheme for reacting flow: I. stiff chemistry, *Journal of Computational Physics* 143 (2) (1998) 381–402.
- [50] J. Bladel, On Helmholtz's theorem in finite regions, Vol. 440, *Midwestern Universities Research Association*, 1958.
- [51] E. Hairer, S. P. Nørsett, G. Wanner, *Solving Ordinary Differential Equations I: Nonstiff Problems*, 2nd Edition, Springer, Berlin, 1993.
- [52] R. J. LeVeque, *Finite Difference Methods for Ordinary and Partial Differential Equations: Steady-State and Time-Dependent Problems*, Society for Industrial and Applied Mathematics (SIAM), Philadelphia, PA, 2007.
- [53] J. H. Ferziger, M. Perić, *Computational methods for fluid dynamics*, Springer, 2002.
- [54] A. Tyliczszak, Projection method for high-order compact schemes for low Mach number flows in enclosures, *International Journal of Numerical Methods for Heat & Fluid Flow* 24 (5) (2014) 1141–1174.
- [55] Y. Morinishi, T. S. Lund, O. V. Vasilyev, P. Moin, Fully conservative higher order finite difference schemes for incompressible flow, *Journal of Computational Physics* 143 (1) (1998) 90–124.
- [56] F. Moukalled, L. Mangani, M. Darwish, *The Finite Volume Method in Computational Fluid Dynamics: An Advanced Introduction with OpenFOAM® and Matlab*, Vol. 113 of *Fluid Mechanics and Its Applications*, Springer, Cham, Switzerland, 2016. doi:10.1007/978-3-319-16874-6.
- [57] K. Rajagopal, Remarks on the notion of “pressure”, *International journal of non-linear mechanics* 71 (2015) 165–172.
- [58] P. M. Gresho, R. L. Sani, On pressure boundary conditions for the incompressible Navier–Stokes equations, *International Journal for Numerical Methods in Fluids* 7 (10) (1987) 1111–1145.
- [59] D. Rempfer, On Boundary Conditions for Incompressible Navier-Stokes Problems, *Applied Mechanics Reviews* 59 (3) (2006) 107–125.
- [60] R. L. Sani, J. Shen, O. Pironneau, P. M. Gresho, Pressure boundary condition for the time-dependent incompressible Navier–Stokes equations, *International Journal for Numerical Methods in Fluids* 50 (6) (2006) 673–682.
- [61] D. Rempfer, Two remarks on a paper by Sani et al., *International Journal for Numerical Methods in Fluids* 56 (10) (2008) 1961–1965.
- [62] J. Kim, P. Moin, Application of a fractional-step method to incompressible Navier–Stokes equations, *Journal of Computational Physics* 59 (2) (1985) 308–323.
- [63] Y. Zang, R. L. Street, J. R. Koseff, A non-staggered grid, fractional step method for time-dependent incompressible Navier–Stokes equations in curvilinear coordinates, *Journal of*

- Computational Physics 114 (1) (1994) 18–33.
- [64] M. Yoon, G. Yoon, C. Min, On solving the singular system arisen from Poisson equation with Neumann boundary condition, *Journal of Scientific Computing* 69 (2016) 391–405.
- [65] S. Abdallah, Numerical solutions for the pressure Poisson equation with Neumann boundary conditions using a non-staggered grid, I, *Journal of Computational Physics* 70 (1) (1987) 182–192.
- [66] W. D. Henshaw, A fourth-order accurate method for the incompressible Navier–Stokes equations on overlapping grids, *Journal of Computational Physics* 113 (1) (1994) 13–25.
- [67] C. Pozrikidis, A note on the regularization of the discrete Poisson–Neumann problem, *Journal of Computational Physics* 172 (2) (2001) 917–923. doi:<https://doi.org/10.1006/jcph.2001.6857>.
- [68] J. Gutiérrez-Jorquera, F. Kummer, A fully coupled high-order discontinuous Galerkin method for diffusion flames in a low-Mach number framework, *International Journal for Numerical Methods in Fluids* 94 (4) (2022) 316–345.
- [69] P. R. Amestoy, I. S. Duff, J.-Y. L’Excellent, J. Koster, MUMPS: a general purpose distributed memory sparse solver, in: *International Workshop on Applied Parallel Computing*, Springer, 2000, pp. 121–130.
- [70] P. R. Amestoy, I. S. Duff, J.-Y. L’Excellent, Multifrontal parallel distributed symmetric and unsymmetric solvers, *Computer Methods in Applied Mechanics and Engineering* 184 (2-4) (2000) 501–520.
- [71] P. J. Roache, *Verification and validation in computational science and engineering*, Vol. 895, Hermosa Albuquerque, NM, 1998.
- [72] G. I. Taylor, A. E. Green, Mechanism of the production of small eddies from large ones, *Proceedings of the Royal Society of London. Series A – Mathematical and Physical Sciences* 158 (895) (1937) 499–521. doi:10.1098/rspa.1937.0036.
- [73] D. L. Brown, R. Cortez, M. L. Minion, Accurate projection methods for the incompressible Navier–Stokes equations, *Journal of Computational Physics* 168 (2) (2001) 464–499.
- [74] E. Fadlun, R. Verzicco, P. Orlandi, J. Mohd-Yusof, Combined immersed-boundary finite-difference methods for three-dimensional complex flow simulations, *Journal of Computational Physics* 161 (1) (2000) 35–60.
- [75] M. Uhlmann, An immersed boundary method with direct forcing for the simulation of particulate flows, *Journal of Computational Physics* 209 (2) (2005) 448–476. doi:<https://doi.org/10.1016/j.jcp.2005.03.017>.
- [76] H. Paillere, C. Viozat, A. Kumbaro, I. Toumi, Comparison of low Mach number models for natural convection problems, *Heat and Mass Transfer* 36 (6) (2000) 567–573.
- [77] J. Vierendeels, B. Merci, E. Dick, Benchmark solutions for the natural convective heat transfer problem in a square cavity with large horizontal temperature differences, *International Journal of Numerical Methods for Heat & Fluid Flow* 13 (8) (2003) 1057–1078.
- [78] F. M. White, *Viscous Fluid Flow*, McGraw-Hill, 1974.
- [79] A. Rohatgi, *Webplotdigitizer* (2024).
URL <https://automeris.io>
- [80] M. P. Severino, M. S. Donini, F. F. Fachini, Mathematical modelling of diffusion flames with continuous geometric variation between counterflow and coflow regimes, *Applied Mathe-*

- matical Modelling 106 (2022) 659–681. doi:10.1016/j.apm.2022.01.019.
- [81] F. F. Fachini, R. P. Bianchin, M. P. Severino, V. M. Sauer, Double Tsuji diffusion flames: Scale analysis, *Combustion Science and Technology* (2025) 1–15doi:10.1080/00102202.2025.2582155.
- [82] M. P. Severino, M. S. Donini, F. F. Fachini, Dynamics of diffusion flames in a very low strain rate flow field: from transient one-dimensional to stationary two-dimensional regime, *Combustion Theory and Modelling* 25 (5) (2021) 861–888. doi:10.1080/13647830.2021.1957155.
- [83] B. Tekgül, H. Kahila, reactingLeFoam, developed at Aalto University, Finland (2020). URL <https://github.com/blttkgl/reactingLeFoam>